



PAPER

Spatio-temporal resolution studies on a highly compact ultrafast electron diffractometer

OPEN ACCESS

RECEIVED

22 December 2014

REVISED

27 February 2015

ACCEPTED FOR PUBLICATION

26 March 2015

PUBLISHED

24 April 2015

C Gerbig, A Senftleben, S Morgenstern, C Sarpe and T Baumert

University of Kassel, Institute of Physics and CINSaT, Heinrich-Plett-Straße 40, D-34132 Kassel, Germany

E-mail: tbaumert@uni-kassel.de**Keywords:** ultrafast electron diffraction, electron pulse characterization, femtosecond electron pulses, spatial coherence, brightness, structural dynamics, multilayer graphene

Content from this work
may be used under the
terms of the [Creative
Commons Attribution 3.0
licence](#).

Any further distribution of
this work must maintain
attribution to the
author(s) and the title of
the work, journal citation
and DOI.

**Abstract**

Time-resolved diffraction with femtosecond electron pulses has become a promising technique to directly provide insights into photo induced primary dynamics at the atomic level in molecules and solids. Ultrashort pulse duration as well as extensive spatial coherence are desired, however, space charge effects complicate the bunching of multiple electrons in a single pulse. We experimentally investigate the interplay between spatial and temporal aspects of resolution limits in ultrafast electron diffraction (UED) on our highly compact transmission electron diffractometer. To that end, the initial source size and charge density of electron bunches are systematically manipulated and the resulting bunch properties at the sample position are fully characterized in terms of lateral coherence, temporal width and diffracted intensity. We obtain a so far not reported measured overall temporal resolution of 130 fs (full width at half maximum) corresponding to 60 fs (root mean square) and transversal coherence lengths up to 20 nm. Instrumental impacts on the effective signal yield in diffraction and electron pulse brightness are discussed as well. The performance of our compact UED setup at selected electron pulse conditions is finally demonstrated in a time-resolved study of lattice heating in multilayer graphene after optical excitation.

1. Introduction

The initial steps in chemical reactions or condensed matter transformations are fundamentally characterized by subnanometer atomic motions on a femto- to picosecond timescale [1, 2]. Time-resolved electron or x-ray diffraction techniques have become a promising tool with sufficient temporal precision to directly deliver insights into ultrafast phenomena at the molecular level [1–4]. Based on the pump–probe approach, ultrashort laser pulses start the reaction dynamics and either x-ray or electron probes are used to provide a time-delayed series of structural diffraction patterns in a stroboscopic manner. Major limitations of these methods have been the photon flux for x-ray sources and the temporal resolution of electron pulses as a result of space charge [1, 2]. Next generation source concepts, such as free-electron lasers and electron diffractometers with RF compression, promise to observe structural dynamics in a single-shot with pulse durations as short as a few fs [4].

Time-resolved diffraction with electron probes intrinsically differs from approaches with x-rays. Electrons possess a considerably higher scattering cross section, which in turn restricts their use to ultrathin samples or surfaces [1–5]. X-ray sources can provide pulses of extraordinary transverse coherence [6], but the shorter wavelength of high-energy electrons can effortlessly resolve interatomic distances [1–5]. However, a main advantage of pulsed electron diffractometers is their relatively small size in comparison to large-scale facilities, such as synchrotrons and free-electron lasers. Ultrafast electron diffraction (UED) table-top apparatuses have been, for example, applied to molecules in the gas phase [7–10], laser-induced melting [11–13], dynamics in graphite [14–19], charge density waves [20, 21], motions in organic salt [22], superstructure dynamics [23] and many others.

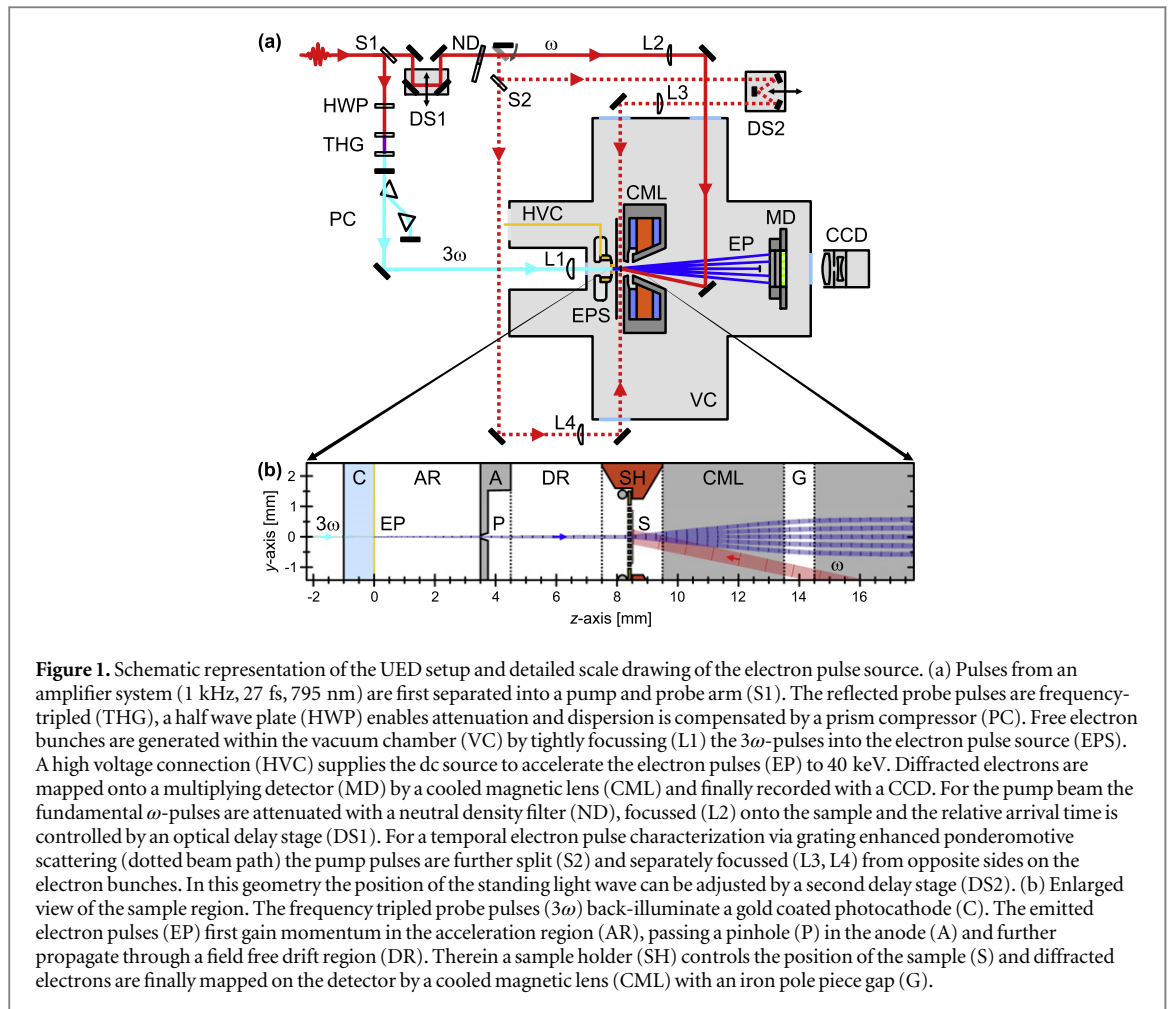
In UED experiments, ultrashort electron pulses are generally created by laser-induced emission. Mainly three different source concepts can be distinguished [5]: Photoelectric emission from planar metal surfaces [7, 15, 24–32], emission from sharp metal tips [33–37] and photo-ionization of ultracold gases [38–42]. Emitted electrons are accelerated either by electrostatic fields to lower energies of 0.2–1.5 keV [33–36] as well as high energies of 30–95 keV [15, 16, 24–32, 37, 42, 43] or with RF photo-injectors up to 3–5 MeV [44–47]. Regardless of the final electron energy, the temporal resolution of a UED setup basically depends on the electrons' initial energy spread, the applied acceleration field strength, the propagation distance to the sample and in particular the charge density of the pulse [1–5, 25]. Coulomb repulsion between the electrons broadens the ultrashort bunches during their propagation from the point of generation to the sample. For bunches containing several electrons, space charge effects therefore limit the minimal electron pulse duration to ~ 200 fs (full width at half maximum (FWHM)) at the sample position [3, 48]. Without additional compression techniques [30–32, 43, 49, 50], a trade-off must be made between the required temporal resolution and the number of electrons per pulse. However, transient diffraction data with an adequate signal-to-noise ratio can only be obtained by detecting 10^6 – 10^8 electrons at each pump–probe delay within a maintainable measurement time [2–5, 43]. Depending on the source concept, different approaches are thus pursued; ranging from the single-electron regime in combination with high repetition rates [5, 35–37, 51], over the application of multi-electron pulses at a lower number of pump–probe cycles [15, 16, 24–29, 42] to single-shot experiments with compressed dense electron bunches [22, 30, 32, 43–47, 50]. In this connection the irreversible or reversible nature of the investigated dynamics additionally determines the method of choice [2, 3, 5].

Apart from the temporal response of an UED experiment, a sufficient spatial resolving capacity of the diffraction patterns is required for achieving atomic resolution, especially of solid systems with large unit cells or complex biomolecules. The evaluation of the spatial resolution is directly connected to a detailed discussion of the electron bunch coherence properties [1–5, 25, 52]. In diffraction the transverse degree of coherence characterizes the interference capability of scattering centres that are far apart. Accordingly, the transverse coherence length of an electron bunch must overlap the entire system under investigation to achieve unrestricted structural information. The longitudinal coherence is of minor impact for uncompressed electron pulses [3, 5, 25, 52]. The transverse coherence length is normally expressed by the electron bunch lateral momentum spread in which global and local momentum distributions must be distinguished [52]. An optimization of the electron emission process can thus improve the coherence by using for example ultracold gases [38–42] or well-tuned laser parameter [51]. Furthermore, a reduction of the electron source size increases the lateral coherence as well, but space charge effects set limits [33–37, 53]. Transverse coherence lengths of 1–5 nm have been reported so far for multi-electron pulses from planar sources with pulse $1/e^2$ -radii of 170–500 μm at the sample [21, 25, 31, 51, 54]. The application of single-electron pulses from a minimized source has recently extended the lateral coherence to 20 nm at a $1/e^2$ -radius of 154 μm [53]. Moreover, the ongoing developments of tip-based [35, 37] and ultracold electron sources [40–42] promise further improvements of the spatial resolution in future challenging UED experiments.

In this contribution, we present extensive spatio-temporal resolution studies on a highly compact ultrafast electron diffractometer by means of experiments and simulations. The focus is here directed towards the robust generation and successful application of uncompressed multi-electron pulses with excellent spatio-temporal properties in the lower space charge regime. In section 2, the experimental details of our UED setup are described and the unique characteristics of the electron source design are pointed out. In section 3, we investigate the interplay between the spatial, temporal and signal resolution and whose impact due to space charge effects and instrumental imperfections. For this purpose, the transverse coherence length is firstly determined in dependence of the electron source size by different methods. Secondly, electron pulses of various charge densities from different source sizes are temporally characterized. Thirdly, the diffraction peak intensity and instrumental brightness are discussed on the basis of previously observed coherence lengths and pulse durations. Finally, the performance of our setup with optimized instrumental parameters is exemplified on the basis of an UED experiment on multilayer graphene. We conclude the contribution with a brief summary.

2. Experimental details

In this section, we describe the experimental details of our UED setup and point out the unique characteristics of the electron pulse source concept, whose performance has been analysed in the spatio-temporal resolution studies presented here. Furthermore, a brief introduction is given to the preparation technique of free-standing single crystalline graphite and graphene samples, which were used for the spatial resolution measurements and time-resolved pump–probe experiments in this work.



2.1. Electron diffraction setup

Experiments in this work were performed with the UED setup illustrated in figure 1(a). The apparatus is powered by a Ti:sapphire multipass amplifier delivering (27 ± 3) fs (FWHM) laser pulses at a central wavelength of 795 nm and $\sim 800 \mu\text{J}$ maximum energy per pulse at a repetition rate of 1 kHz. Beam pointing and output power are independently stabilized by a closed-loop control system. The laser pulses are first separated into a pump and probe beam, each continuously adjustable in power via a neutral density filter and half-wave plate respectively. The reflected $\sim 40 \mu\text{J}$ probe pulses are frequency-tripled to a central wavelength of (267 ± 2) nm and a maximum energy of ~ 200 nJ per pulse by third-harmonic generation in nonlinear crystals. Present dispersion is compensated within a dual pass prism compressor. SD-FROG measurements [55] verified a minimal UV pulse duration of (30 ± 4) fs (FWHM). Photoelectron pulse emission takes place within a UHV chamber (pressure $< 10^{-9}$ mbar) by back-illuminating a gold coated sapphire cathode (40 nm vapour-deposited Au with 3 nm Ni–Cr adhesive layer on 1 mm thin sapphire plate). The combination of a re-entrant view port construction and a lens with short focal distance ($f = +60$ mm) opens the possibility to adjust the $1/e^2$ -radius of the electron source between $2.3 \mu\text{m}$ and $30 \mu\text{m}$. After emission, the electron pulses are accelerated to a kinetic energy of 40 keV across a gap of (3.5 ± 0.2) mm from the isolated high voltage cathode to the grounded anode (see figure 1(b)). The high static electric field strength of (11.4 ± 0.7) MV m^{-1} is achievable with carefully polished stainless steel electrodes and a pressed in, glue-free implementation of the sapphire cathode. The accelerated electron pulses pass a pinhole of $100 \mu\text{m}$ diameter, which is drilled in the anode, and further propagate through a 5 mm field free drift region. This contains a 2 mm thin copper sample holder, which is adjustable in six axes and offers eight slots for standard TEM grids. After sample transmission, a liquid cooled magnetic lens with iron pole-pieces separated by a 1 mm vacuum gap maps the diffraction pattern on the detector system. Compared to dc electron sources with a condenser solenoid in front of the sample [15, 24–29], we place the magnetic lens afterwards as an object lens and focus the full diffraction pattern on the detector [17]. This results in an extraordinary short propagation distance from the electron source to the sample of 8.5 mm, a trifold improvement to the so far most compact source design [26, 48]. Diffracted electrons are finally multiplied by a chevron stack of micro-channel plates and imaged on a P43 scintillator screen, which is located

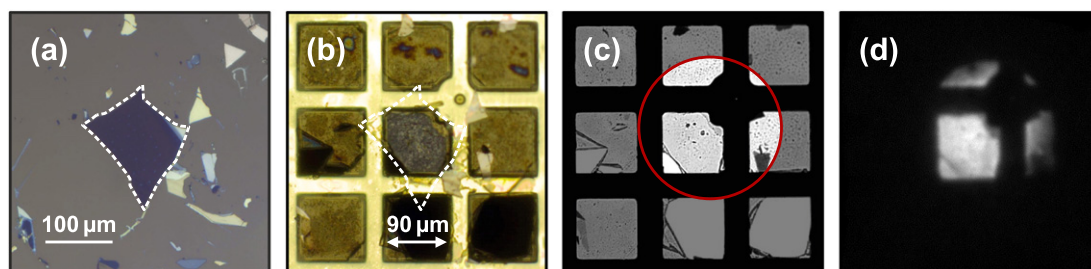


Figure 2. Single crystalline multilayer graphene sample. (a) Optical micrograph of a nine layer graphene flake (dashed outline) on a Si/SiO₂ substrate. (b) Optical reflection image of the transferred free-standing graphene flake (dashed line) on a Quantifoil 200 mesh gold grid. (c) Optical transmission image of the sample shown in (b). The highlighted area (red circle) indicates the transmission region in (d). (d) Shadowgraph of the sample with 40 keV electron pulses.

188 mm away from the electron source. A charge-coupled device (CCD) records the resulting pattern with one megapixel resolution. The number of electrons per pulse can be measured by an aluminium faraday cup and a pico-amperemeter.

Performing time-resolved pump–probe experiments the sample is excited by the fundamental of the amplifier system at 795 nm. Dispersion management after the amplifier for UV pulse generation and for propagation to the sample is adjusted such, that a pulse duration of (27 ± 3) fs (FWHM) is achieved in front of the sample. A long focal lens ($f = +500$ mm) focuses the p-polarized laser pulses with 12° angle of incidence onto the sample. The beam is slightly over-focussed to avoid effects due to beam pointing and inhomogeneous excitation of $\sim 100 \mu\text{m}$ large samples (see figure 2). The spot size at the sample position was determined by a CCD beam profiler giving a $1/e^2$ -diameter of $\sim 480 \mu\text{m}$ (see section 3.4 and figure 13(d) for details). The incident fluence is continuously variable via a reflecting neutral density filter and a maximum peak fluence of $\sim 60 \text{ mJ cm}^{-2}$ can be used at the sample position in pump–probe experiments. A high precision optical delay stage controls the relative arrival time between the electron probe and optical pump pulse. By recording diffraction pattern snapshots at different time delays, laser induced structural dynamics in the sample can be observed directly.

The overall time resolution under normal incidence of electrons to the sample is mainly limited due to the electron pulse duration, which is further influenced by internal space charge effects and the initial energy spread. For a temporal pulse characterization, the electron bunches are directly cross-correlated with two counter-propagating laser pulses. This method uses the ponderomotive force of the pulsed laser field acting on the electrons in a standing-wave enhanced geometry [30, 31, 48]. As illustrated in figure 1 (a) (dotted beam line), the fundamental pump pulses are splitted once again and are separately focussed ($f = +300$ mm) with a $1/e^2$ - radius of $33 \mu\text{m}$ and energy of $\sim 200 \mu\text{J}$ per pulse at the electron bunches in a counter-propagating way. The position of the resulting stationary light wave is adjusted with the help of a second delay stage. By finally measuring the ponderomotively scattered electrons at different delay times on the detector, the local electron pulse charge density at a definite point in time and space can be reconstructed (see section 3.2 for details).

2.2. Single crystalline graphite and graphene sample preparation

Free-standing single crystalline graphite and graphene samples have been prepared in a three-step procedure (see [56] for details). First, macroscopic single crystal flakes of natural graphite are cleaved by multiple mechanical exfoliation with semiconductor grade adhesive tape [57]. The thinned graphite is afterwards deposited on top of an oxidized silicon wafer and its surface is carefully scanned in an optical microscope (see figure 2(a)). In the second step, residual flakes of adequate size and thickness are characterized by optical reflection [58] as well as atomic force microscopy, giving the possibility to directly count the number of graphene layers. In the final step, a selected flake is transferred on top of a Quantifoil 200 mesh TEM gold grid ($90 \mu\text{m}$ hole size, see figure 2(b)). For an improved transfer process, the grid is partially covered by a perforated carbon film [56]. This amorphous support film is selectively removed from the sample grid hole before preparation by fs laser machining to reduce the electron diffraction background signal and avoid perturbing effects in pump–probe experiments. All experimental results shown in sections 3.1, 3.3 and 3.4 have been achieved using the 3 nm thick, nine layer graphene sample shown in figure 2.

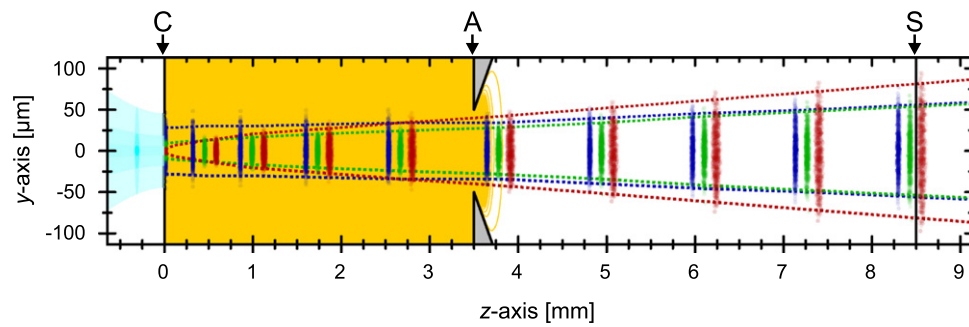


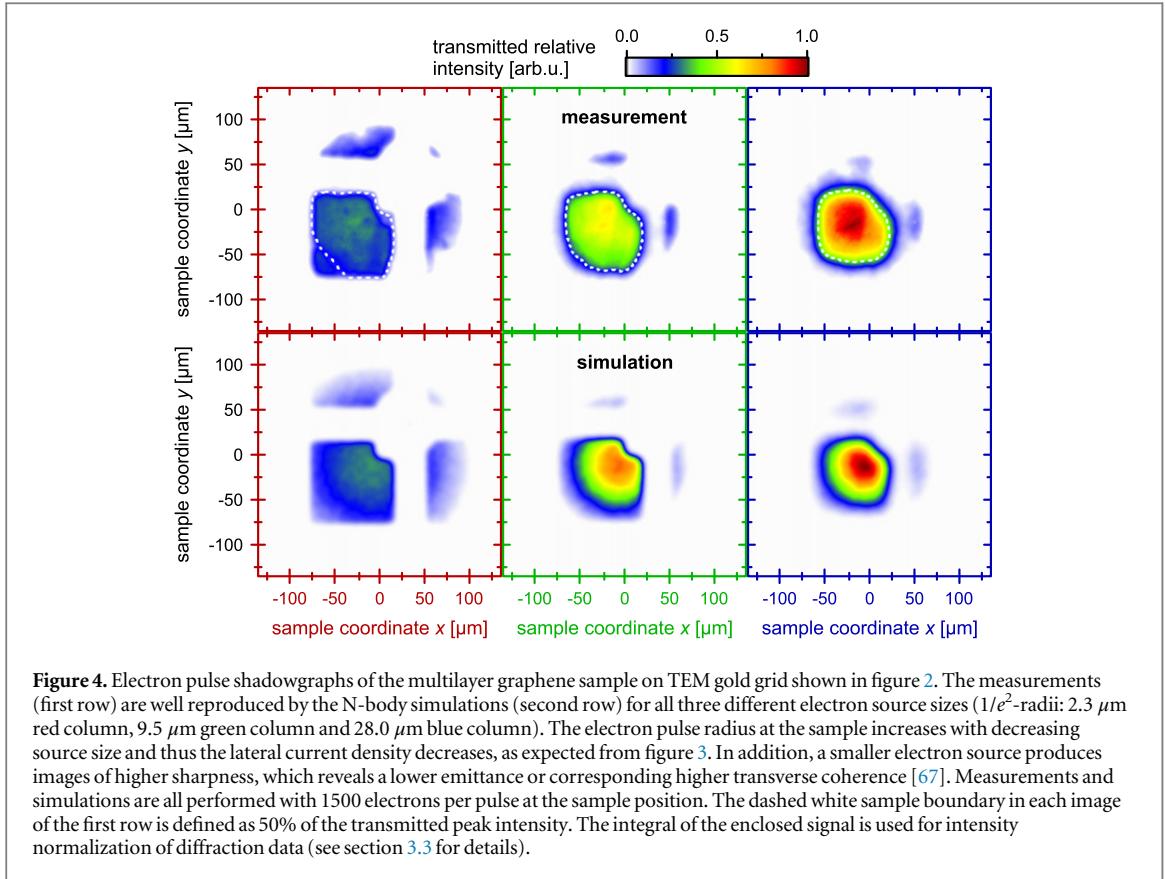
Figure 3. Simulated propagation of electron pulses from the cathode (C) to the sample (S) for three different electron source sizes ($1/e^2$ -radii: $2.3 \mu\text{m}$ red pulses, $9.5 \mu\text{m}$ green pulses and $28.0 \mu\text{m}$ blue pulses). The evolution of the $1/e^2$ -diameters (dotted lines) is predominantly affected by source sized dependent space charge forces and a negative lens effect induced due to the inhomogeneous penetration of the electric potential (yellow contour) into the field-free drift region (A \rightarrow S). The simulations were all performed with 1500 electrons per pulse and snapshots were taken in time steps of 10 ps. The positions of red and blue pulses are offset by $\pm 130 \mu\text{m}$ for visibility.

3. Results and discussion

In experiments and simulations, we have investigated the transverse coherence length, electron pulse duration, elastic scattered peak intensity and instrumental peak brightness in dependence of the electron pulse charge density. For this purpose three spot sizes of the UV probe beam on the photocathode were chosen. The lateral profiles of the UV beam were measured with a scanning knife-edge method at three defined longitudinal beam positions: directly at the beam waist, 0.5 mm behind the waist and 3 mm in front. Provided that the beam profile had an overall Gaussian shape, the corresponding $1/e^2$ -radii were: $(2.3 \pm 0.5) \mu\text{m}$, $(9.5 \pm 1.3) \mu\text{m}$ and $(28.0 \pm 1.2) \mu\text{m}$ respectively. A pointing jitter of the laser focus was not observed, but would be included in the measured results that were averaged over many shots. The electron emission is a single-photon process and thus permits to transfer the measured optical quantities linearly onto the electron source. Consequently, a simple adjustment of the longitudinal position of the UV pulse focussing lens (see figure 1(a)) allows a variation of the electron source area over more than two orders of magnitude. For all source sizes the emitted charge from the photocathode were measured to be linear in dependence of the UV laser power without saturation effects in the studied parameter range. Hence, the electron pulse emission is below the space charge limited regime and the virtual cathode effect has not been taking into account [59, 60]. For clarity, all source size dependent results presented in the following figures are colour-coded as follows: $2.3 \mu\text{m}$ source in red, $9.5 \mu\text{m}$ source in green and $28.0 \mu\text{m}$ source in blue.

3.1. Transverse coherence length

We have characterized the transverse coherence length of our UED setup for the mentioned three electron source sizes with particle tracking simulations and three experimental approaches. The N-body simulation was self-developed to get direct access to all tuneable parameters and their effects on the spatio-temporal resolution of the UED experiment (for simulation details see appendix B). Figure 3 displays the evolution of the electron bunch diameter from the generation at the cathode to the sample position for each of the three source sizes. The transverse dynamics of the electron pulses can be separated into two effects. Mainly during the acceleration, space charge forces cause a nonlinear expansion of the bunches, which strongly depend on the initial electron charge density. Still inside the acceleration region, the pulse diameters thus become almost equal for all three different source sizes. After the bunches pass the anode pinhole, the expansion is enhanced by the inhomogeneous penetration of the electric field into the field-free drift region. The pinhole acts like a negative lens and increases the bunch diameters linearly during further propagation [51]. Finally, at the sample position, the electron pulses basically represent a magnified image of their spatial distributions at the cathode. For a fixed electron gun design the magnification thus depends just on the strength of acting space charge effects, which can be influenced by the initial electron source size and the number of emitted electrons per pulse. In addition to the lateral expansion of the electron pulses during propagation, the global degree of coherence is enlarged similarly. In other words, the ratio of bunch radius to coherence length is conserved and the electron pulse transverse coherence can be approximated with knowledge of the initial coherence properties at the cathode [53]. From an analytical expression of the thermal emittance for metal cathodes [61–63], we expect an initial transverse coherence length of $\xi_1 = (0.67 \pm 0.16) \text{ nm}$ for our electron pulse source, which is consistent with comparable



values reported for gold cathodes [51, 53, 64] (see appendix B.1 for details). Thereby, the transverse coherence length at the sample ξ_s can be valued from

$$\xi_s \leq \xi_i \frac{w_s}{w_i}, \quad (1)$$

with the electron source $1/e^2$ -radius w_i and electron pulse $1/e^2$ -radius w_s at the sample [53]. Equality in equation (1) holds in the absence of space charge effects. Accordingly, we can get an upper limit of the electron pulses transverse coherence lengths at the sample position by measuring the ratio w_s/w_i for all three different electron source sizes. The source radii w_i are mentioned above and the corresponding radii at the sample w_s were determined from electron shadowgraphs as shown in the upper image row of figure 4. Therefore, the electron pulses were imaged onto the detector with the magnetic lens switched off. Using the shadow of the TEM sample grid (shown in figure 2) as a length gauge, the radii at the sample w_s were calculated by the second central moment of the radial intensity profiles on the detector, resulting in $1/e^2$ -radii of $w_{s,2.3} = (84.7 \pm 12.3)\ \mu\text{m}$, $w_{s,9.5} = (64.4 \pm 10.9)\ \mu\text{m}$ and $w_{s,28.0} = (57.4 \pm 10.4)\ \mu\text{m}$. From equation (1) we finally estimated transverse coherence lengths at the sample position of $\xi_{s,2.3} < (24.7 \pm 14.8)$, $\xi_{s,9.5} < (4.5 \pm 2.5)$ and $\xi_{s,28.0} < (1.2 \pm 0.6)$ nm.

Furthermore, the N-body simulations have been utilized to confirm the predicted transverse coherences for all three source sizes. Results of the simulated electron pulse intensity profiles are presented in the lower image row of figure 4 and show a good agreement with the experimental outcomes. It should be noted, that no free parameters were used in the simulations (see appendix B for details). The particle tracking algorithm makes the 6D phase-space distribution of an electron pulse accessible during propagation and allows to calculate the transverse normalized root mean square (RMS) emittance

$$\epsilon_{n,x} \equiv \frac{1}{m_0 c} \sqrt{\langle x^2 \rangle \langle p_x^2 \rangle - \langle x p_x \rangle^2}, \quad (2)$$

with the particle coordinate x , relativistic momentum p_x , electron rest mass m_0 and speed of light c . The brackets $\langle \rangle$ stand for averaging over the entire particle ensemble of the bunch and the transverse emittance $\epsilon_{n,y}$ in y -direction is given analogously [54, 65, 66]. Due to the cylindrical symmetry of our electron bunches we maintain $\epsilon_{n,x} = \epsilon_{n,y} = \epsilon$ from the source to the sample. From simulations of all three source sizes we obtained mean transverse emittance values at the sample position of $\epsilon_{s,2.3} = (0.8 \pm 0.1)$ nm, $\epsilon_{s,9.5} = (2.6 \pm 0.4)$ nm and $\epsilon_{s,28.0} = (7.5 \pm 0.3)$ nm for the three source radii of $2.3\ \mu\text{m}$, $9.5\ \mu\text{m}$ and $28.0\ \mu\text{m}$, respectively. Moreover, the

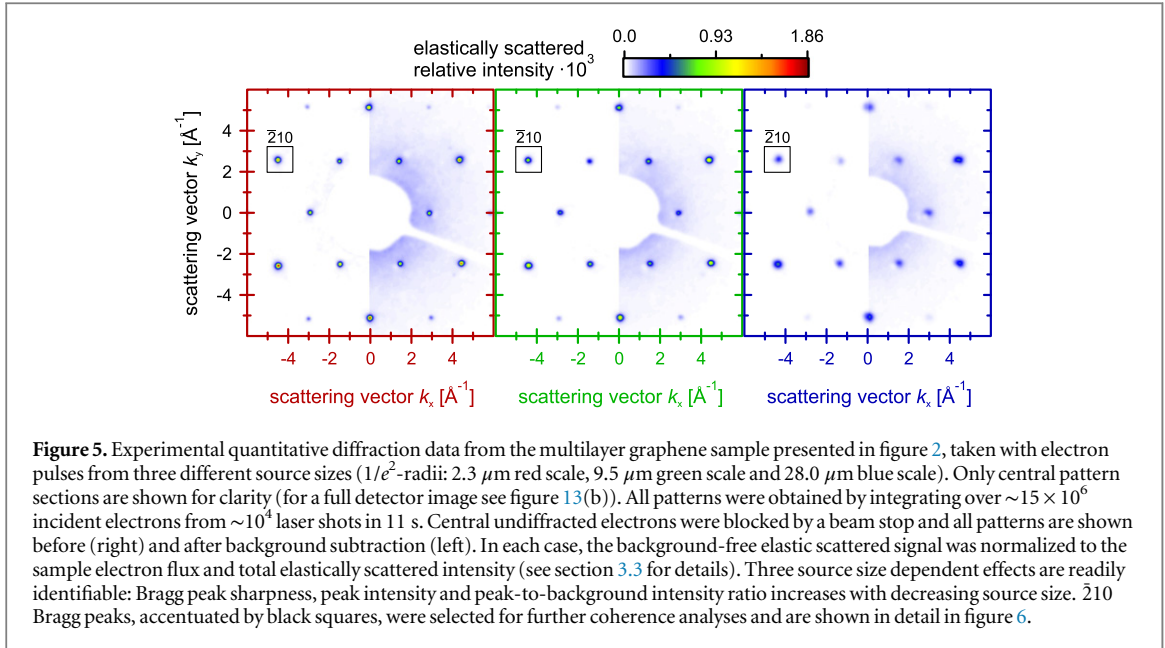


Figure 5. Experimental quantitative diffraction data from the multilayer graphene sample presented in figure 2, taken with electron pulses from three different source sizes ($1/e^2$ -radii: 2.3 μm red scale, 9.5 μm green scale and 28.0 μm blue scale). Only central pattern sections are shown for clarity (for a full detector image see figure 13(b)). All patterns were obtained by integrating over $\sim 15 \times 10^6$ incident electrons from $\sim 10^4$ laser shots in 11 s. Central undiffracted electrons were blocked by a beam stop and all patterns are shown before (right) and after background subtraction (left). In each case, the background-free elastic scattered signal was normalized to the sample electron flux and total elastically scattered intensity (see section 3.3 for details). Three source size dependent effects are readily identifiable: Bragg peak sharpness, peak intensity and peak-to-background intensity ratio increases with decreasing source size. 210 Bragg peaks, accentuated by black squares, were selected for further coherence analyses and are shown in detail in figure 6.

transverse coherence length ξ_s can be estimated from the transverse normalized RMS emittance ε_s by

$$\xi_s \approx \frac{\hbar}{m_0 c} \frac{w_s}{2\varepsilon_s}, \quad (3)$$

where \hbar is the reduced Planck constant [54, 65] (see appendix A for details). With equations (2) and (3), the particle tracking simulations for all three source sizes result in mean transverse coherence lengths at the sample position of $\xi_{s,2.3} \approx (19.2 \pm 2.6)$ nm, $\xi_{s,9.5} \approx (3.8 \pm 0.6)$ nm and $\xi_{s,28.0} \approx (1.45 \pm 0.04)$ nm. Consequently, the simulated coherence properties are well consistent with the coherence values determined by the source expansion ratio giving an upper limit.

A direct experimental access to the transverse emittance and hence to the transverse coherence is provided by pepper-pot or multislit techniques [68]. In accordance with [67], we analysed TEM grid shadowgraphs as shown in figure 4 by fitting error functions to the intensity profile of a grid edge. Taking the detector point spread function (PSF) (see figure 8 and corresponding text) into account through deconvolution [67], we obtained mean transverse coherence lengths at the sample of $\xi_{s,2.3} = (14.6 \pm 6.2)$ nm, $\xi_{s,9.5} = (2.9 \pm 0.2)$ nm and $\xi_{s,28.0} = (1.3 \pm 0.1)$ nm. The results of the TEM grid method are thus slightly below the previous coherence lengths specified by the source expansion ratio and simulated emittance. The main reason for the deviations is attributed to space charge broadening of the edge profile during the bunch propagation from the grid to the detector. Additionally, mechanical vibrations of the sample holder could reduce the edge sharpness of the TEM grid shadowgraphs. This method sets therefore a lower boundary to the measured transverse coherence.

However, the transverse coherence length of electron pulses not only limits the maximum resolvable distance in a sample, it further quantifies the resolution of the electron diffraction pattern in reciprocal space. More precisely, an increasing transverse coherence ξ_s narrows the width of Bragg peaks in a pattern proportionally by

$$\xi_s = \frac{1}{\sigma_k}, \quad (4)$$

where σ_k is the standard deviation for Gaussian distributed Bragg peaks (see appendix A for details). Thus, we measured diffraction data for the three selected electron source sizes and extracted the particular transverse coherence from the respective peak width. Figure 5 presents the recorded diffraction signals, which were acquired from the multilayer graphene sample shown in figure 2 by integrating in 11 s over $\sim 10^4$ electron pulses with 1500 electrons per pulse. Due to a source size dependent divergence angle of the electron bunches at the sample (see figure 3), the focussing current of the magnetic lens was optimized for each source condition to the narrowest Bragg peak width. The central undiffracted electron signal was not considered and permanently blocked by a copper beam stop to avoid detector degradation. All recorded diffraction patterns were individually separated from the diffuse background which was approximated by a circular bi-exponential function (see patterns in figure 5) and subsequently interpolated onto a reciprocal grid with a common scale. Afterwards, the residual elastic scattered signals were normalized to the sample electron flux and total elastic scattered intensity (see section 3.3 for details). First of all, the resulting diffraction data basically show three effects with increasing

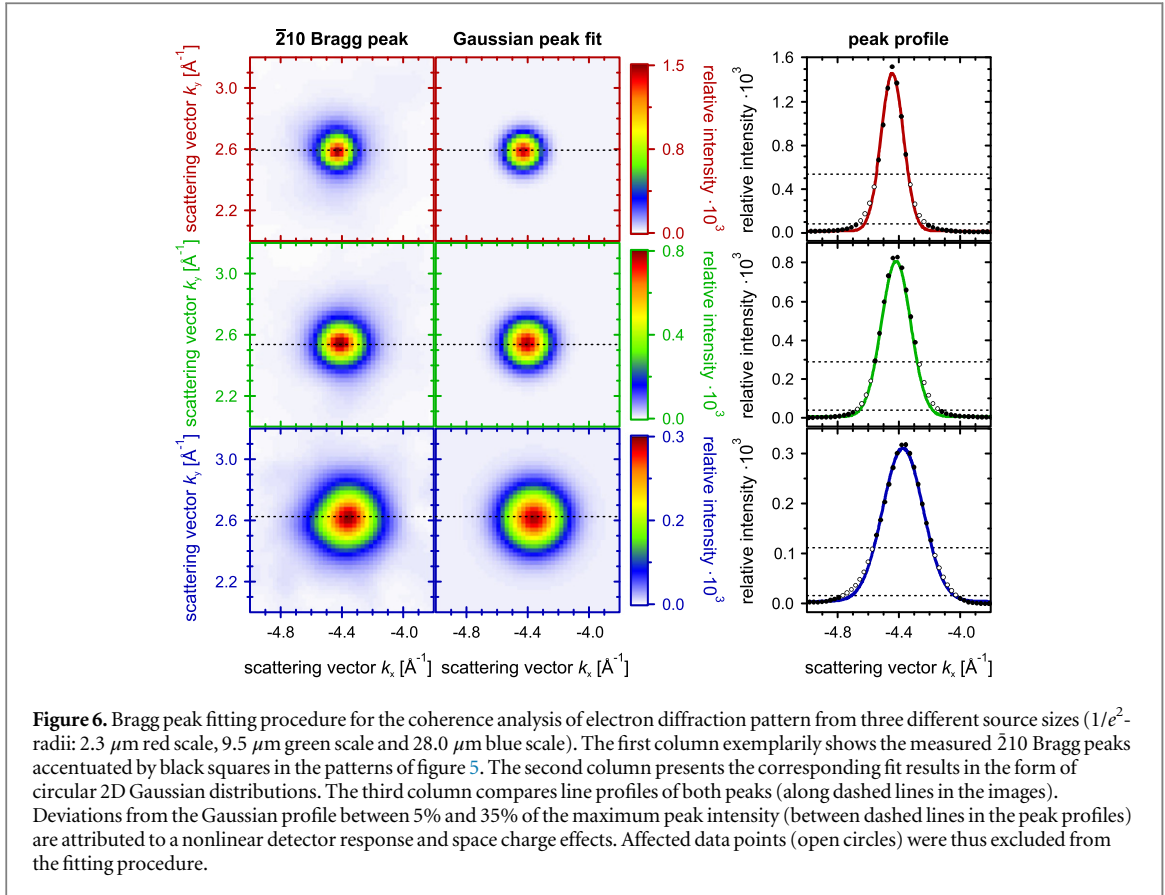


Figure 6. Bragg peak fitting procedure for the coherence analysis of electron diffraction pattern from three different source sizes ($1/e^2$ -radii: $2.3 \mu\text{m}$ red scale, $9.5 \mu\text{m}$ green scale and $28.0 \mu\text{m}$ blue scale). The first column exemplarily shows the measured $\bar{2}10$ Bragg peaks accentuated by black squares in the patterns of figure 5. The second column presents the corresponding fit results in the form of circular 2D Gaussian distributions. The third column compares line profiles of both peaks (along dashed lines in the images). Deviations from the Gaussian profile between 5% and 35% of the maximum peak intensity (between dashed lines in the peak profiles) are attributed to a nonlinear detector response and space charge effects. Affected data points (open circles) were thus excluded from the fitting procedure.

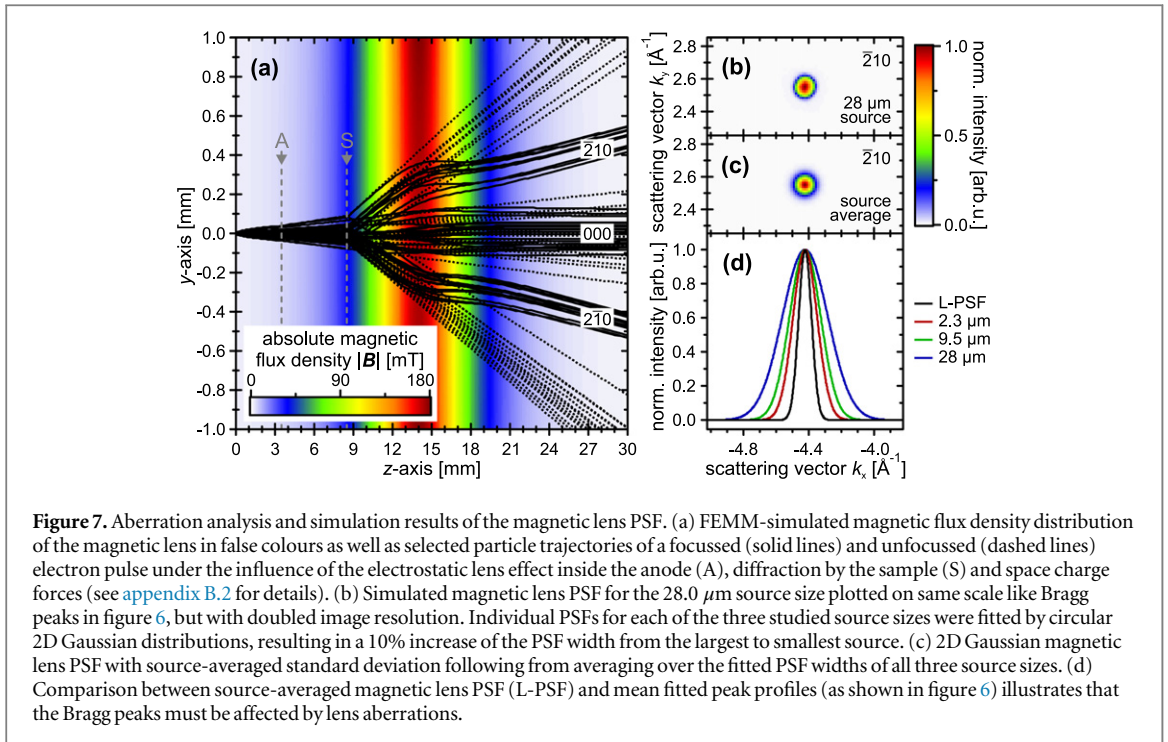
source size: The Bragg peak width increases as expected and the peak intensity thus decreases (see also figure 6). Although the diffuse background is stronger for the smallest source due to the fact that more electrons transmitted the sample surrounding amorphous carbon film (see figures 2 and 4), the elastically scattered signal can be separated better from the background and the signal-to-noise ratio consequently increases with decreasing source size.

To further extract the transverse coherence for all three source sizes from the Bragg peak width, we fitted in each case a circular 2D Gaussian function to a series of peaks in a pattern. Figure 6 exemplifies the fitting procedure for the $\bar{2}10$ Bragg peaks accentuated by black frames in the patterns of figure 5. All intensity profiles are well approximated by the circular 2D Gaussian distribution. Minor deviations only exist between 5% and 35% of the maximum peak intensity (see dashed lines in the peak profiles of figure 6). This spreading of the measured peak tails arises from space charge effects and a nonlinear signal response, which is attributed to artefacts in the detector imaging system [69–71]. Data points affected from this broadening were therefore disregarded in the fitting procedure. Accordingly, we analysed the 24 most intense Bragg peaks in each pattern, resulting in an averaged peak standard deviation of $\sigma_{k,I,2.3} = (0.727 \pm 0.009) \text{nm}^{-1}$, $\sigma_{k,I,9.5} = (0.924 \pm 0.008) \text{nm}^{-1}$ and $\sigma_{k,I,28.0} = (1.344 \pm 0.016) \text{nm}^{-1}$. The corresponding instrumental transverse coherence lengths $\xi_{1,2.3} = (1.38 \pm 0.01) \text{nm}$, $\xi_{1,9.5} = (1.08 \pm 0.01) \text{nm}$ and $\xi_{1,28.0} = (0.74 \pm 0.01) \text{nm}$ were finally calculated from equation (4). It is obvious that these results differ from already ascertained coherence values. Most notably the expected scaling of the Bragg peak width with the source size was not reproduced. Consequently, the resolution of the electron diffraction patterns must be essentially affected by instrumental imperfections [71, 72]. We have taken in account two well-known basic causes: aberrations of the magnetic electron lens [71, 72] and signal spreading in the detector system [71, 73, 74]. For each effect, a 2D PSF was determined in reciprocal space to further deconvolute the measured Bragg peak width [72]. Afterwards, the source-limited transverse coherence length ξ_s at the sample can be extracted from the mean instrumental Bragg peak width $\sigma_{k,I}$ by

$$\xi_s = \frac{1}{\sqrt{\sigma_{k,I}^2 - \sigma_{k,L}^2 - \sigma_{k,D}^2}}, \quad (5)$$

with the magnetic lens PSF width $\sigma_{k,L}$ and detector PSF width $\sigma_{k,D}$ (standard deviations).

The magnetic lens PSF represents a focussed image of an electron point source onto the detector under aberrations and space charge effects. Especially within the space charge regime, an ideal electron point source is not experimentally realizable. Therefore, we determined the magnetic lens PSF by simulating the magnetic field



distribution of the solenoid with the freely available FEMM finite element program [75] and performed particle tracking simulations with implemented magnetic field. Figure 7(a) exemplifies projected particle trajectories of an electron pulse generated from the 2.3 μm source with (solid lines) and without (dashed lines) acting magnetic field in combination with the magnetic flux density distribution. The particle tracking algorithm additionally includes diffraction from $\bar{2}10$ and $2\bar{1}0$ lattice planes in the multilayer graphene sample (see also figure 13(b)), the negative lens effect of the anode pinhole and space charge forces. The strength of lens aberrations and thus the width of the magnetic lens PSF basically depends on the abaxial electron pulse properties inside the solenoid field. Consequently, we separately determined a magnetic lens PSF for each of three studied source sizes due to their different electron pulse lateral diameters and divergence angles (as shown in figure 3). Additionally, the strong abaxial particle trajectories of diffracted electrons were taken into account by implementing the scattering process at the sample representatively in $\bar{2}10$ direction. In order to finally obtain the source size dependent magnetic lens PSFs, the $\bar{2}10$ Bragg peak intensity distribution on the detector was separately simulated based on a focussed electron point source with the abaxial properties of the particular finite source (see appendix B.2 for details). Figure 7(b) exemplarily presents the resulting magnetic lens PSF for the 28.0 μm electron source. Standard deviations $\sigma_{k,L}$ for all three source sizes were determined by fitting each simulated lens PSF with a circular 2D Gaussian distribution. The results show a 10% increase of the PSF width from the largest to smallest source size due to stronger aberrations of electron pulses from the smallest source with an eventually larger lateral diameter and divergence angle. The source-averaged Gaussian lens PSF possesses a standard deviation of $\sigma_{k,L} = (0.395 \pm 0.028) \text{ nm}^{-1}$ and is shown in figure 7(c) on the same scale like Bragg peaks in figure 6. For a clear comparison, the line profile of the source-averaged magnetic lens PSF is shown together with the mean diffraction peak profiles of all three source sizes in figure 7(d). Especially for the smallest 2.3 μm source, the lens PSF width represents 54% of the corresponding Bragg peak width. Consequentially, magnetic lens aberrations have to be taken into account to reconstruct the source-limited transverse coherence length from the diffraction pattern resolution.

We analysed the lateral signal spreading of the detector system according to [73, 74]. The detector PSF was estimated to be a 2D Gaussian distribution and its width was determined by fitting circular 2D Gaussians to single-electron detector events. For this purpose, the electron beam was mapped on the detector with removed sample grid and inactive magnetic lens. Images were recorded under same conditions as diffraction patterns in figure 5. Statistically occurring detector events around the central beam have been associated with single electrons scattered from the anode pinhole. The signal could be clearly distinguished from general detector dark counts when the electron emission by the UV laser pulses was interrupted. We finally evaluated nine separate image sections around the central electron spot. Figure 8(a) presents one of the utilized sections with single-electron events. A total of 419 events were individually fitted by a circular 2D Gaussian distribution, resulting in an averaged detector PSF standard deviation of $\sigma_{k,D} = (0.556 \pm 0.006) \text{ nm}^{-1}$. The lower row in figure 8(a) (below

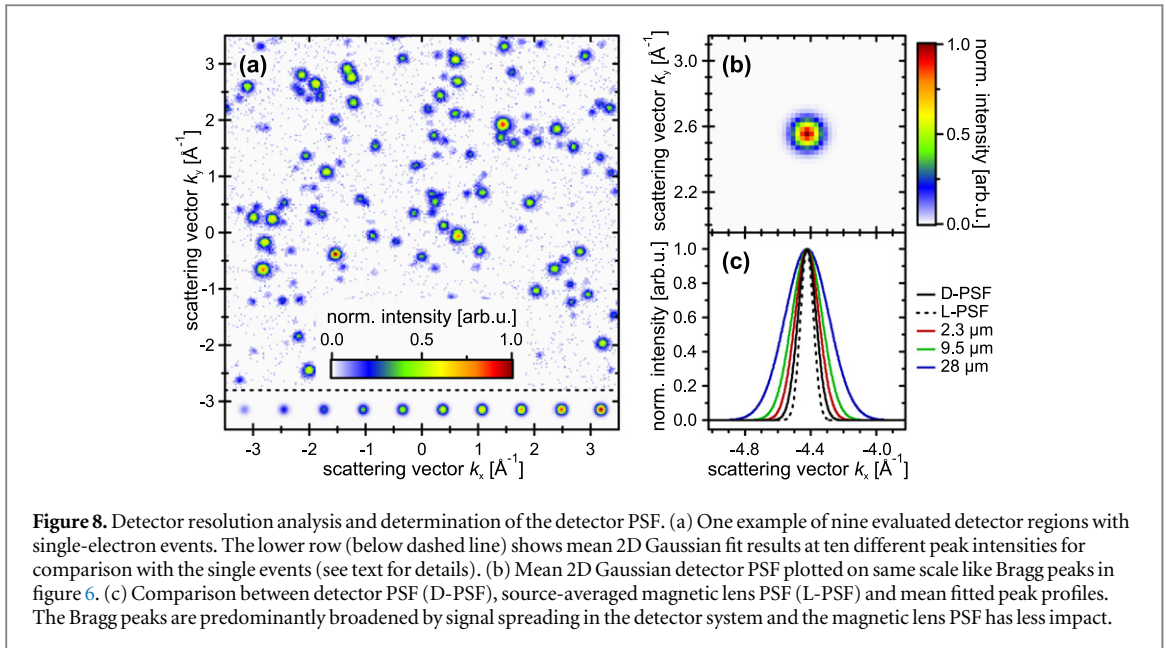


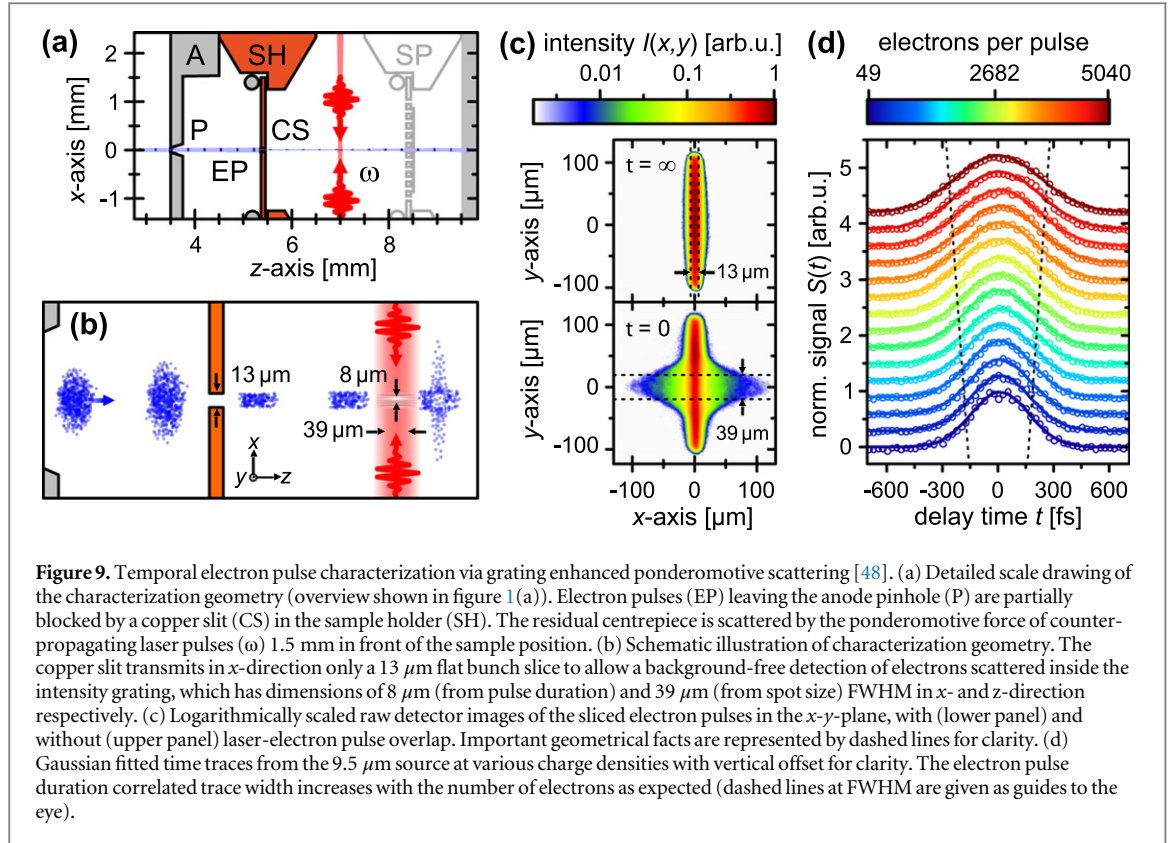
Table 1. Comparison of different approaches and their corresponding results to the transverse coherence length for three altered electron pulse source sizes.

Source size (μm)	Transverse coherence length (nm)			
	Via source expansion (upper limit)	Via simulated emittance	Via TEM grid method (lower limit)	Via deconvoluted Bragg peak width
2.3 ± 0.5	24.7 ± 14.8	19.2 ± 2.6	14.6 ± 6.2	10.0 ± 14.4
9.5 ± 1.3	4.5 ± 2.5	3.8 ± 0.6	2.9 ± 0.2	1.6 ± 0.1
28.0 ± 1.2	1.2 ± 0.6	1.45 ± 0.04	1.3 ± 0.1	0.85 ± 0.01

the dashed line) displays averages of the fitted PSFs for 10 different peak intensities, which agree well with the corresponding measured single events. The variation in the signal gain is well known for micro-channel plate detectors and characterized by the width of the pulse height distribution [76]. A first comparison between the detector PSF in figure 8(b) and the magnetic lens PSF in figure 7(c) (both plotted on same scale) already demonstrates, that the major impact on the Bragg peak broadening is attributed to the signal spreading in the detector system. The line profiles in figure 8(c) provide a direct assessment of the detector PSF, magnetic lens PSF and mean diffraction peak widths. The detector PSF width represents 76% of the Bragg peak width in case of the smallest source size in contrast to 54% for the lens PSF. Deconvolution reveals that aberrations of the magnetic lens and the signal spreading in the detector causes a sevenfold broadening of the Bragg peaks for the $2.3 \mu\text{m}$ source. Finally, we calculated for all three source sizes the source-limited transverse coherence lengths $\xi_{s,2.3} = (10.0 \pm 14.4) \text{ nm}$, $\xi_{s,9.5} = (1.6 \pm 0.1) \text{ nm}$ and $\xi_{s,28.0} = (0.85 \pm 0.01) \text{ nm}$ from equation (5). Although instrumental imperfections have been taken into account, those outcomes are consistently smaller than values obtained by the other methods. We attribute the deviations to additional broadening effects like fluctuations in the magnetic lens current, a lack of sample flatness, crystal strains and inhomogeneities [71, 72]. Thus, the full information content of complex electron diffraction patterns could only be partially retrieved with the quantitative knowledge of detector and magnetic lens PSFs [72].

Table 1 summarizes the four different approaches and their results to the transverse coherence length for all three analysed electron source sizes. Therefore, our highly compact electron source design can provide 1500 electrons in a single pulse at the sample with a transverse coherence up to 20 nm while maintaining a small bunch $1/e^2$ -radius of less than $85 \mu\text{m}$. This will open the opportunity to study biomolecular or solid samples with large unit cells, which was so far only achievable in the single-electron regime using a planar cathode [53] or sharp metal tips [33–37] as well as with ultracold electron sources [38–42].

However, a reduction of the source size to improve the lateral coherence inevitably comes along with a temporal pulse broadening due to increasing space charge forces. Consequently, we further investigated the electron pulse duration as a function of the number of electrons per pulse for all three different source sizes.



3.2. Temporal electron pulse characterization

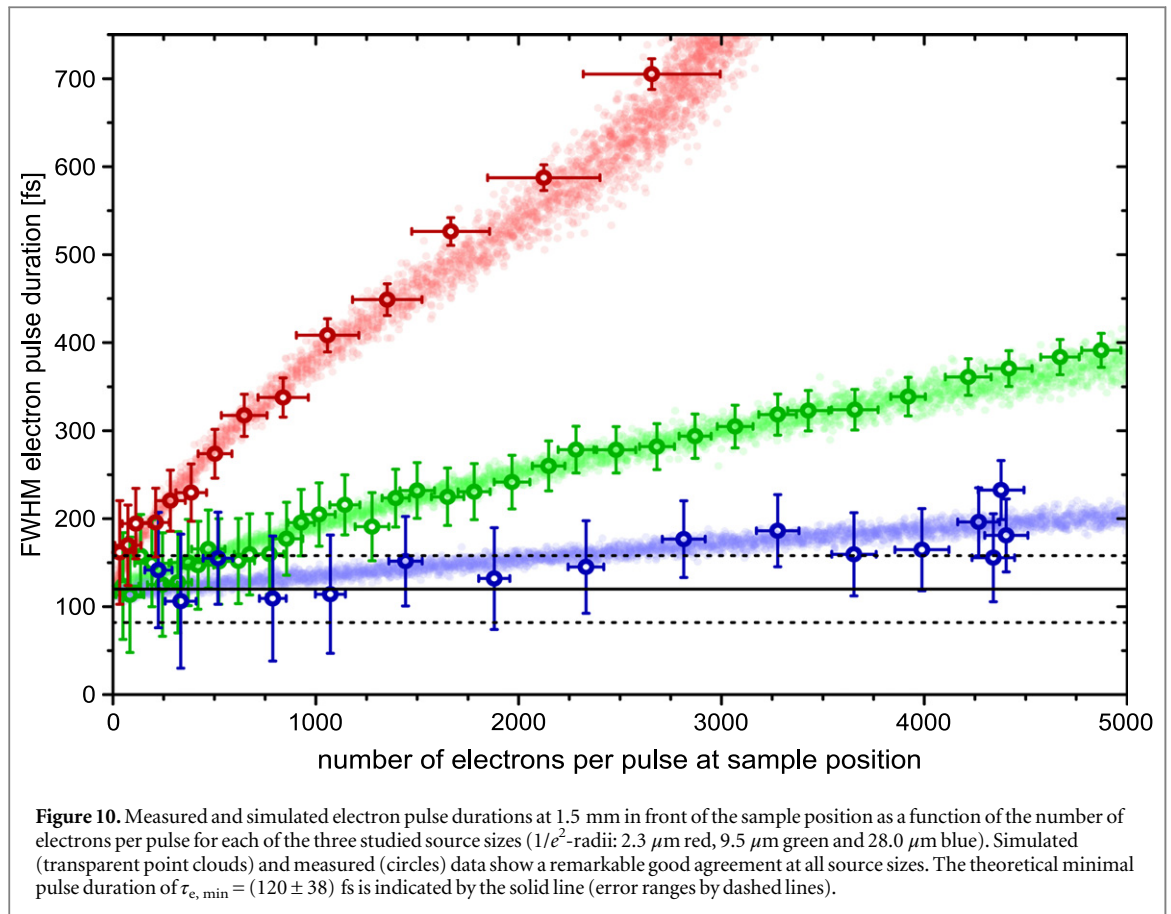
Different approaches are used for measuring the temporal profile of ultrashort electron bunches in table-top experiments [29, 48, 77, 78]. In our UED setup we have characterized electron pulse durations by grating enhanced ponderomotive scattering according to [30, 31, 48, 79]. This cross-correlation method uses the ponderomotive interaction of the electron bunches with two counter-propagating laser pulses in a standing-wave enhanced geometry (see figure 9(b)). By measuring the ponderomotively scattered electron signal at different delay times on the detector, the FWHM of the electron pulse duration τ_e can be reconstructed from FWHM τ_s of the signal time trace (see figure 9(d)) by

$$\tau_e = \sqrt{\tau_s^2 - \tau_f^2 - \tau_l^2}, \quad (6)$$

with the laser pulse duration τ_l and the FWHM focal transit time τ_f of the electron pulse through the joint laser focus. For a comprehensive description of the grating enhanced ponderomotive scattering technique see [48]. We have experimentally realized the characterization method as illustrated in figure 1 (a) (dotted beam line) and detailed in figures 9(a) and (b). The fundamental pump pulses were split to $\sim 200 \mu\text{J}$ per pulse and separately focussed ($f = +300 \text{ mm}$) to a spot size of $\Omega = (39 \pm 2) \mu\text{m}$ (FWHM) onto the electron bunches. The focal intersection was placed as close as possible to the sample position (1.5 mm in front) to achieve a meaningful estimation of the electron pulse duration in pump–probe experiments. A correct retrieval of the electron pulse duration was just acquirable by a background-free detection of scattering signal. For this purpose, electron pulses leaving the anode were centrally sliced by a 13 μm narrow copper slit before the residual centre part was scattered by the ponderomotive force of the standing-wave laser field (see figure 9(b)). Figure 9(c) shows logarithmically scaled detector images of the sliced electron pulses at the optimal temporal laser–electron pulse overlap at time zero (bottom) and in absence of the ponderomotive force (top). The background-free detection provides to measure the scattering signal over more than two orders of magnitude. To further extract the electron pulse duration from image data at various time delays t , we used the method from [31, 48] as follows: The scattering signal S at delay time t is given by integrating the pixel intensities $I(x, y, t)$ weighted by the scattered distance x from the slice centre,

$$S(t) = \int |x| I(x, y, t) dx dy. \quad (7)$$

Figure 9(d) exemplifies resulting signal time traces $S(t)$ of electron pulses from the 9.5 μm source at different charge densities. The trace widths, which are correlated with electron pulse durations, already show a clear broadening (indicated by the dashed lines) with the number of carriers per pulse as expected due to increasing



space charge forces. By fitting Gaussian functions to the time traces, we obtained in each case an electron pulse duration τ_e from the FWHM τ_s of the trace fit by means of equation (6) with the focal transit time $\tau_f = (346 \pm 21)$ fs (FWHM) and laser pulse duration $\tau_l = (27 \pm 3)$ fs. The transit time $\tau_f = \Omega/v_z$ is given by the focal spot size Ω and the mean electron longitudinal velocity $v_z = 112 \text{ nm fs}^{-1}$. For instance, the evaluation of the lowermost and topmost signal time trace in figure 9(d) resulted in FWHM electron pulse durations of (120 ± 62) fs and (410 ± 18) fs for 49 ± 79 and 5040 ± 102 electrons per pulse, respectively. Convolved with the pump pulse duration of 12 fs (RMS) and the 22 fs (RMS) effect of the non-collinear sample excitation, these values correspond to RMS temporal resolutions of (57 ± 28) fs and (176 ± 9) fs.

For a detailed quantification of the temporal pulse broadening with decreasing electron source size, we have investigated the electron pulse duration for the three studied sources as a function of the number of particles per pulse. Results of the ponderomotive scattering experiment in combination with simulated electron pulse durations are presented in figure 10. Calculated (transparent point clouds) and measured (circles) data are in remarkable good agreement. The simulated pulse durations were computed by the particle tracking algorithm used in section 3.1. The good agreement with the measured results was only achievable by a rigorous implementation of all experimental parameter including the copper slit as well. Mainly two effects can lead to deviations between the measured pulse duration of the sliced electron pulses 1.5 mm in front of the sample position and the actual pulse duration of the unsliced electron pulses used for UED experiments. First, space charge effects can broaden the temporal pulse profile under further propagation to the sample and the measured electron pulse duration would be underestimated. However, the temporal characterization was only performed at the central part of the nearly Gaussian electron pulse profile which is more affected by space charge broadening than the electron pulse edges. This fact causes an overestimation of the pulse duration. In consideration of both opposite aspects, our simulations could finally reveal that the slicing effect is more significant and the unsliced pulse duration at the sample can be up to 6% shorter in comparison to the measured pulse duration. It should be noted, that no free parameters were used in all simulations of electron pulse durations (see appendix B for details).

The results of the temporal pulse characterization in figure 10 show that for all source sizes a minimal electron pulse duration of ~ 120 fs can be reached with less than 50 electrons per pulse close to the single-electron regime. This value is supported by theoretical considerations from [25, 51], providing a minimal pulse duration of $\tau_{e, \text{min}} = (120 \pm 38)$ fs for our instrumental parameters.

Above ~ 50 electrons per pulse in the presence of space charge effects, the strength of the temporal pulse broadening strongly depends on the source size. Electron pulses with (2814 ± 14) carriers (more than sufficient to study reversible dynamics) still remain ultrashort with a FWHM pulse duration of (175 ± 44) fs in case of the largest $28.0 \mu\text{m}$ source, whereas they are strongly broadened to (705 ± 17) fs for the smallest $2.3 \mu\text{m}$ source with (2656 ± 338) electrons per pulse. The fourfold growth in pulse duration is put into perspective by taking into account that the initial charge density increases by more than two orders of magnitude. Furthermore, the drastically enhanced transverse coherence of electron pulses from the smallest source implicates increasing diffraction peak intensities (see figure 5 and section 3.3 for details) and allows a reduction of the number of electrons per pulse. For instance, diffraction patterns with excellent signal-to-noise ratio as presented in figure 13(b) are achievable within a minute exposure time using either (839 ± 124) electrons per pulse from the $2.3 \mu\text{m}$ source or (1500 ± 85) electrons from $9.5 \mu\text{m}$ source. Thus, FWHM pulse durations of (337 ± 17) fs or (230 ± 32) fs in combination with transverse coherence lengths up to 20 or 4 nm, respectively become applicable for high-precision UED experiments. Our comprehensive spatio-temporal resolution studies consequently reveal that the compactness of our electron source design provides at balanced conditions a temporal resolution of less than 200 fs along with high-definition electron diffraction.

3.3. Coherence-dependent diffraction peak intensity and instrumental brightness

As already indicated, the transverse coherence length of electron pulses not only defines the Bragg peak width in diffraction patterns (see section 3.1 for details), it consequentially affects the Bragg peak intensity at a steady electron flux through the sample. More precisely, the peak intensity of a Bragg spot increases quadratically with its underlying transverse coherence [52, 71]. To investigate this correlation, we analysed the diffraction peak intensity in dependence of the transverse coherence length for each of the three studied source sizes.

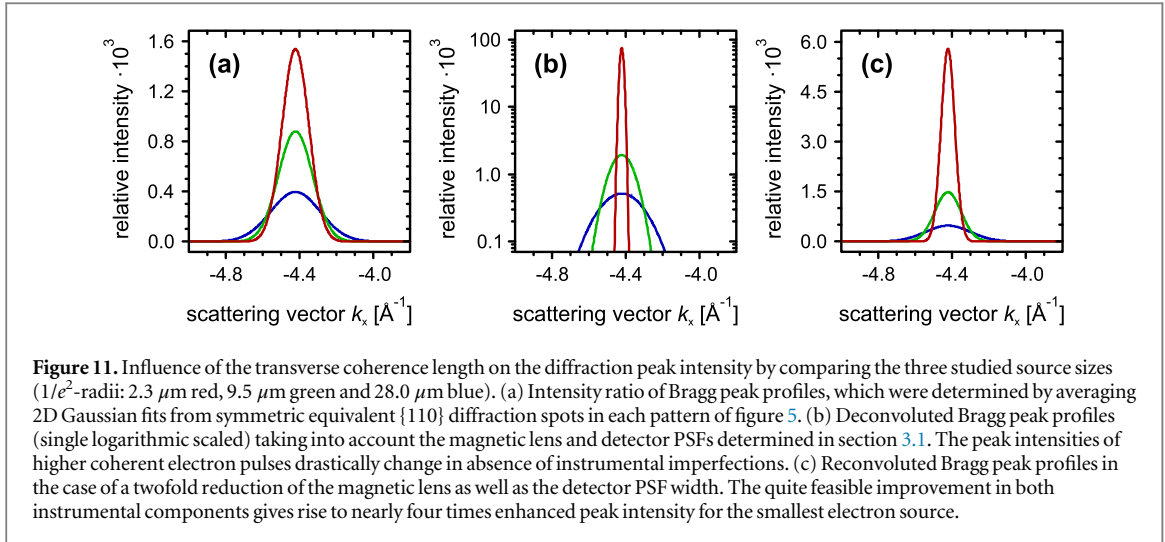
For this purpose, raw pattern images had to be normalized after background subtraction to obtain the quantitative diffraction data shown in figure 5. As each individual diffracted electron in a bunch only interferes with itself [5, 51, 71] and its scattering probability is mainly determined by sample intrinsic parameters [25, 71], we first normalized each background-free pattern $I_{\text{bf}}(k_x, k_y)$ by its overall elastic scattered intensity

$$I_n(k_x, k_y) = \frac{I_{\text{bf}}(k_x, k_y)}{\iint I_{\text{bf}}(k_x, k_y) dk_x dk_y}, \quad (8)$$

to eliminate disturbing influences due to laser and electron source fluctuations during the recording process. Afterwards, each standardized diffraction pattern $I_n(k_x, k_y)$ was normalized by its particular incident electron flux at the sample as follows: We determined the source-size dependent flux by analysing the sample shadowgraphs presented in the first image row of figure 4. For each image, pixel values below 50% of the maximum transmitted intensity were set to zero and the remaining entire intensity was integrated. The 50% threshold facilitates for all three images a strict distinction between directly transmitted and scattered electrons (not visible in figure 4) by means of sharp boundary conditions (indicated by dashed lines in figure 4). The outcomes were normalized relative to the largest $28.0 \mu\text{m}$ source, resulting in a relative electron flux of 61% and 82% for the $2.3 \mu\text{m}$ and $9.5 \mu\text{m}$ source, respectively. The standardized diffraction pattern $I_n(k_x, k_y)$ were finally divided by the relative electron flux values to obtain a consistent intensity scale for the diffraction data of all three studied source sizes presented in figure 5.

To reveal a potential quadratic dependence of the Bragg spot peak intensity on the transverse coherence length, we fitted the 110 and similar five permutation symmetric $\{110\}$ Bragg spots (equal distances to the centre) in all three quantitative diffraction patterns by 2D Gaussian distributions (see section 3.1 and figure 6 for fit details). Averaging over the six fits from each of the three patterns provided the Gaussian peak profiles presented in figure 11(a). The direct comparison clearly shows a rise of the peak intensity with increasing transverse coherence. The $2.3 \mu\text{m}$ and $9.5 \mu\text{m}$ source achieves a 3.9 or 2.2 times higher peak intensity relative to the $28.0 \mu\text{m}$ source. However, a quadratic intensity dependence should result in a relative peak intensity enhancement by a factor of 138.4 or 3.5 assuming the deconvoluted transverse coherence lengths of 10.0 nm and 1.6 nm, respectively (see table 1). In order to check, we deconvoluted the 2D Gaussian distribution corresponding to the peak profiles in figure 11(a) with the magnetic lens PSF and the detector PSF (compare section 3.1). The 2D deconvolution was performed under conservation of the total peak volume. Figure 11(b) illustrates resultant profiles of the source-limited Bragg peaks on a single logarithmic scale. Their intensity and width drastically change for higher coherent electron pulses in absence of instrumental imperfections. The deconvoluted peak intensities of the $2.3 \mu\text{m}$ and $9.5 \mu\text{m}$ source are 144.6 and 3.7 times higher with respect to the $28.0 \mu\text{m}$ source and in good agreement with the expected ones (see above).

Furthermore, we analysed the peak intensity ratio in case of a prospective minimization of magnetic lens aberrations and signal broadening effects in the detector system. For this purpose, the source-limited Bragg peaks were reconvoluted by a magnetic lens PSF as well as a detector PSF, which both have half the widths of the



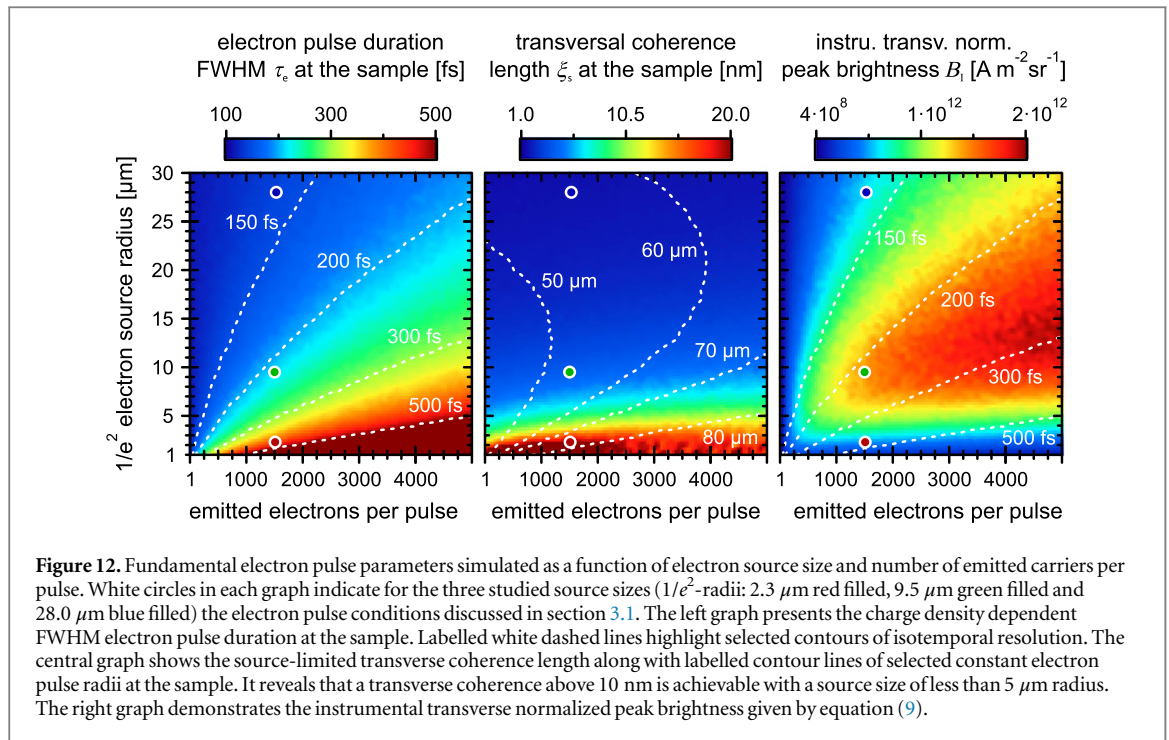
obtained PSFs in section 3.1. The 2D reconvolution was again calculated under conservation of the total peak volume. Figure 11(c) presents the resultant Bragg peak profiles. This quite feasible improvement in both instrumental components would give rise to a 12.1 and 3.1 times higher peak intensity for the 2.3 μm and 9.5 μm source relative to the 28.0 μm source. The peak intensity for the smallest electron source would be nearly four times enhanced and the spatial resolution considerably improved in contrast to our current experimental conditions.

So far our comprehensive resolution studies have shown that all spatial and temporal electron pulse parameters can be reliably retrieved by theoretical considerations and numerical simulations. With respect to an optimized performance of time-resolved diffraction experiments, we finally introduce the transverse beam brightness, which is the most often used figure of merit for the electron pulse quality in applications where the longitudinal energy spread is of minor importance [66]. To account for the above-mentioned decrease of Bragg peak intensities due to instrumental imperfections, the magnetic lens and detector PSFs are included in the brightness definition. Accordingly, we have calculated the instrumental transverse normalized peak brightness B_1 in our cylindrically symmetric setup as follows:

$$B_1 \approx \left(\frac{m_0 c}{\pi \hbar} \right)^2 \sqrt{\frac{8 \ln 2}{2\pi}} \frac{N e \xi_1^2}{\tau_e w_s^2}, \quad (9)$$

where ξ_1 is the instrumental transverse coherence length affected by instrumental imperfections, w_s is the lateral electron pulse $1/e^2$ -radius at the sample, τ_e is the FWHM electron pulse duration, N is the number of electrons per pulse at the sample, \hbar is the reduced Planck constant, e is the elementary charge, m_0 is the electron rest mass and c the speed of light (see appendix B.3 for derivation details). The instrumental transverse brightness B_1 represents a figure of merit for the acquirable diffraction signal yield in space at a given resolution in time. We therefore simulated the instrumental brightness as a function of the electron source size and number of emitted electrons per pulse to obtain an ideal electron pulse setting for UED experiments. First, electron pulse durations τ_e and source-limited transverse coherence lengths ξ_s were simulated by means of our particle tracking algorithm. Corresponding outcomes are summarized in figure 12. The pulse duration changes as expected and already discussed in section 3.2. The results of the lateral coherent properties reveal that a source-limited transverse coherence length ξ_s above 10 nm is achievable in our setup with an electron source radius of less than 5 μm . Furthermore, we convoluted coherence values ξ_s with the magnetic lens and detector PSFs from section 3.1. Separate calculations of individual magnetic lens PSFs for each of the simulated electron pulse settings were not included. Finally, the instrumental brightnesses B_1 were determined by equation (9). The right-hand graph in figure 12 shows the simulated result. It clearly demonstrates for our UED setup that smaller sources with radii below 5 μm indeed reach highest transverse coherences; the instrumental brightness however is less in comparison to larger sources. Reasons for this are enlarged pulse radii, longer pulse durations and less electrons per pulse at the sample that are all caused by intensified space charge forces. The higher transverse coherence of a smaller source would only shift the brightness distribution downwards with a significant improvement of both the magnetic lens and detector resolution as mentioned above.

However, the instrumental brightness graph in figure 12 demonstrates that the highest signal yield in combination with a short pulse duration as well as enhanced transverse coherence is achieved in case of the 9.5 μm source size and 1500 emitted electrons per pulse (indicated by a green filled white circle in the graph).



3.4. Performance-optimized time-resolved experiment on multilayer graphene

The performance of our highly compact ultrafast electron diffractometer is lastly exemplified in a time-resolved diffraction experiment with optimized electron pulse parameters. We have observed the in-plane lattice heating in multilayer graphene after fs laser excitation and analysed the results by means of the Debye–Waller theory according to [16].

The multilayer graphene sample shown in figure 2 was excited optically at the fundamental wavelength of the amplifier system with a mean incident fluence of $(6.2 \pm 0.4) \text{ mJ cm}^{-2}$ at a pulse duration of $(27 \pm 3) \text{ fs}$ (FWHM) (see section 2.1 for experimental details). Lattice dynamics were probed by electron pulses from the 9.5 μm source with 1500 ± 50 electrons per pulse at the sample and measured pulse durations of $(230 \pm 32) \text{ fs}$ (FWHM). High-definition diffraction patterns were recorded at 271 time delay values with variable temporal increments from -30 ps before to 200 ps after laser excitation. Each delay step was approached a hundred times to average out short-term laser and instrumental fluctuations. For each approach, the diffraction patterns of 660 laser shots were added up. Consequently, a total exposure time of 66 s or $\sim 10^8$ electrons were accumulated for each delay value, resulting in an overall measurement time of 12.5 h for time-resolved data at highest quality. Figure 13(b) exemplifies a resultant diffraction pattern at negative time delay.

For evaluation of the transient diffraction data, a total number of 101 Bragg peaks up to a lattice vector of $|\mathbf{G}| = 18.4 \text{ \AA}^{-1}$ were first indexed as shown in figure 13(b). Some diffraction spots were not considered due to perturbing stray light from the pump laser. Afterwards, each selected Bragg peak was individually fitted within a rectangular image section (indicated by squares in figure 13(b)) by a 2D Gaussian distribution (see section 3.1 and figure 6 for fit details). The fitting procedure enables the time-resolved analysis of the peak intensity and moreover a sub-pixel determination of the peak width and position. To give an impression of the instrumental performance, we will only focus on intensity changes in the following.

The evolution of peak intensities after laser excitation is exemplarily illustrated in figure 13(a) by six selected Bragg peaks in [210] direction of the direct lattice. The dynamics clearly show a fast and a slow decay component and were thus fitted by bi-exponential decay functions (indicated by solid lines) according to [16]. A complete evaluation of the transient diffraction data resulted in mean time constants of $(444 \pm 16) \text{ fs}$ and $(11.8 \pm 0.2) \text{ ps}$ for the fast and slow decay, respectively. The small error limits point out the high data quality and large number of analysable Bragg peaks. The underlying physical processes in graphite and graphene have been widely investigated and are still under debate [14–19, 80–85]. However, a detailed discussion of phonon decay mechanisms goes beyond the scope of this paper and will be presented elsewhere.

The inset in figure 13(a) exemplifies the excellent setup performance on basis of the residual from fitted 110 Bragg peak intensity dynamics (not shown in the main graph). Assuming that the peak intensity decay is perfectly described by the bi-exponential fit function, the residual represents an upper limit of the diffraction signal noise. A statistical analysis of the residual (indicated by the histogram on the right) resulted in an overall signal noise below $\pm 0.23\%$ (standard deviation). Taking a mean intensity drop of 6.54% for the 110 peak into

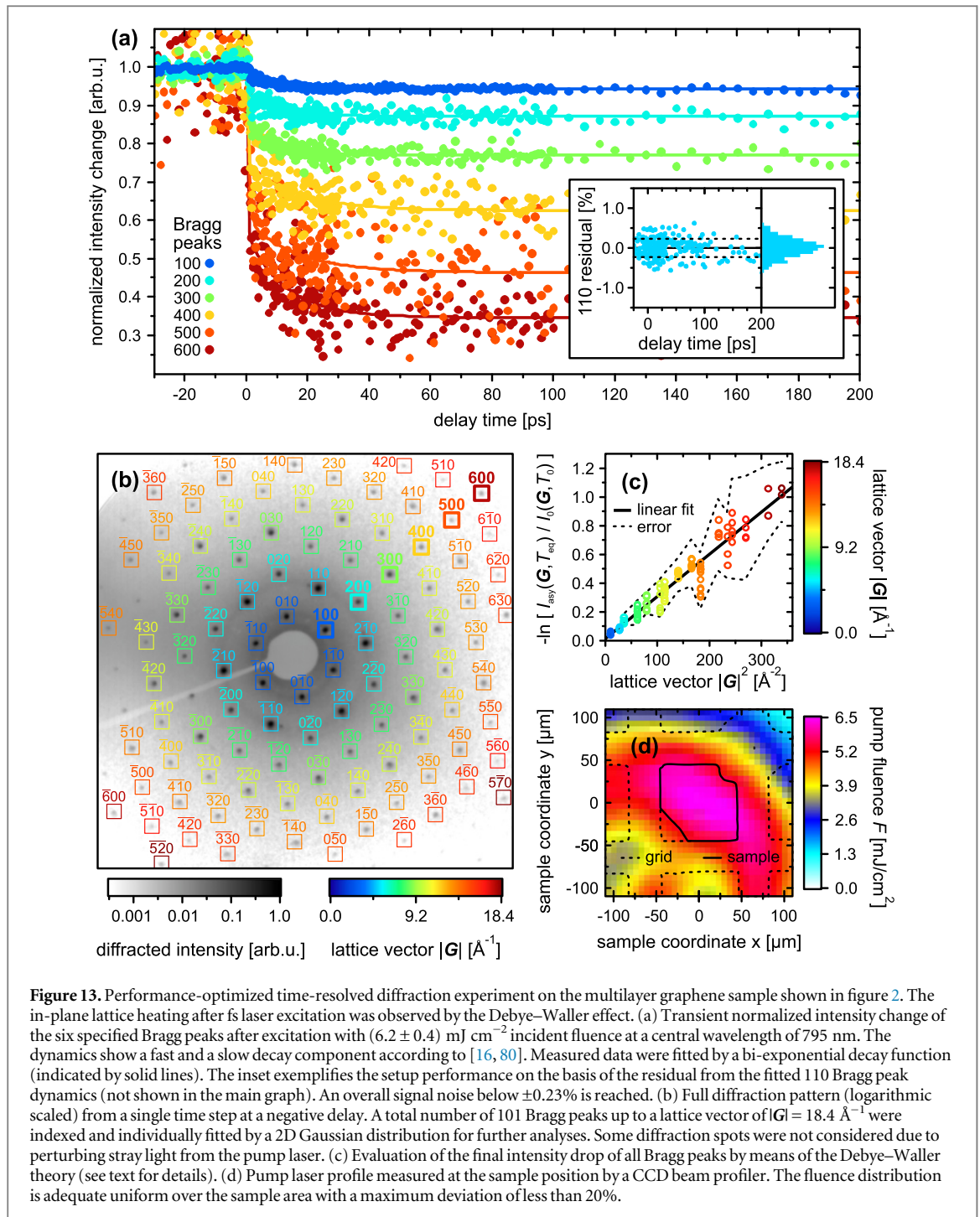


Figure 13. Performance-optimized time-resolved diffraction experiment on the multilayer graphene sample shown in figure 2. The in-plane lattice heating after fs laser excitation was observed by the Debye–Waller effect. (a) Transient normalized intensity change of the six specified Bragg peaks after excitation with $(6.2 \pm 0.4) \text{ mJ cm}^{-2}$ incident fluence at a central wavelength of 795 nm. The dynamics show a fast and a slow decay component according to [16, 80]. Measured data were fitted by a bi-exponential decay function (indicated by solid lines). The inset exemplifies the setup performance on the basis of the residual of the fitted 110 Bragg peak dynamics (not shown in the main graph). An overall signal noise below $\pm 0.23\%$ is reached. (b) Full diffraction pattern (logarithmic scaled) from a single time step at a negative delay. A total number of 101 Bragg peaks up to a lattice vector of $|G| = 18.4 \text{ \AA}^{-1}$ were indexed and individually fitted by a 2D Gaussian distribution for further analyses. Some diffraction spots were not considered due to perturbing stray light from the pump laser. (c) Evaluation of the final intensity drop of all Bragg peaks by means of the Debye–Waller theory (see text for details). (d) Pump laser profile measured at the sample position by a CCD beam profiler. The fluence distribution is adequate uniform over the sample area with a maximum deviation of less than 20%.

account, a signal-to-noise ratio above 28 can thus be reached in time-resolved diffraction experiments. It should be additionally noted that the 3 nm thin graphene sample only provides a weak diffraction signal and the estimated signal-to-noise ratio therefore demonstrates a lower limit of the instrumental performance.

Finally, we evaluated the asymptotic intensity decrease of all indexed Bragg peaks in figure 13(b) to give an impression of the analysable amount of diffraction data and its quality. A recent UED study on a 1–3 nm thin graphite film [16] concluded that the thermal equilibrium is reached around 150 ps after laser excitation, which is in compliance with our results at comparable pump fluences. In addition, the final lattice temperature rise could be well reconstructed from both the intensity reduction of Bragg peaks combined with the Debye–Waller theory as well as from calculations including the absorbed laser fluence and temperature-dependent heat capacity of graphite. In the following, we determined the final lattice temperature of our sample first due to the Debye–Waller theory and secondly from the absorbed pump fluence according to [16].

The intensity of a Bragg peak $I(\mathbf{G}, T)$ is reduced for a given reciprocal lattice vector \mathbf{G} and temperature T by the Debye–Waller factor, usually defined as $\exp[-2W(\mathbf{G}, T)]$. The equilibrium lattice temperature $T_{\text{eq}} = T_0 + \Delta T$

can thus be calculated from the asymptotic Bragg peak intensity $I_{\text{asy}}(\mathbf{G}, T_{\text{eq}})$ by $\ln[I_{\text{asy}}(\mathbf{G}, T_{\text{eq}})/I_0(\mathbf{G}, T_0)] = -2 [W(\mathbf{G}, T_{\text{eq}}) - W(\mathbf{G}, T_0)]$ with the initial Bragg peak intensity $I_0(\mathbf{G}, T_0)$ at room temperature $T_0 = (296 \pm 3)$ K. Assuming that the measured Bragg peaks in figure 13(b) with Miller indices $hk0$ mostly represent in-plane lattice dynamics and the corresponding in-plane Debye temperature θ_D is considerably higher than the final temperature rise ΔT , $W(\mathbf{G}, T)$ is given by

$$W(\mathbf{G}, T) = \frac{1}{4} |\mathbf{G}|^2 \langle u_{\text{in}}^2 \rangle = \frac{1}{4} |\mathbf{G}|^2 \frac{6\hbar^2}{m_C k_b \theta_D} \left[\frac{1}{4} + \left(\frac{T}{\theta_D} \right)^2 \int_0^{\theta_D/T} \frac{\epsilon}{e^\epsilon - 1} d\epsilon \right], \quad (10)$$

where $\langle u_{\text{in}}^2 \rangle = \langle u_x^2 \rangle + \langle u_y^2 \rangle$ is the temperature-dependent in-plane atomic mean square displacement, m_C is the mass of a carbon atom, k_b is the Boltzmann constant and \hbar is the reduced Planck constant [16, 86, 87]. Therefore, we plotted the relative intensity decrease $-\ln[I_{\text{asy}}(\mathbf{G}, T_{\text{eq}})/I_0(\mathbf{G}, T_0)]$ for all indexed Bragg peaks against the square of the absolute value of the reciprocal lattice vector $|\mathbf{G}|^2$ and fitted the data set by a linear regression with weighting due to the errors of $I_{\text{asy}}(\mathbf{G}, T_{\text{eq}})$. Figure 13(c) illustrates the corresponding results. The slope of the linear regression was further used as a constraint to solve equation (10) by additionally taking into account a temperature dependence of the in-plane Debye temperature with $\theta_D(T_0) = 1330$ K [87] and $\theta_D(T_{\text{eq}}) = 1627$ K [87, 88]. The theoretical temperature behaviour of the Debye temperature was adapted from [88] and scaled onto the experimental value at room temperature [87]. Thus, we finally obtained a laser-induced heating of the multilayer graphene sample to an equilibrium temperature of $T_{\text{eq}} = (1234 \pm 19)$ K. This precise temperature determination within the applied theoretical approximations could be achieved mainly by the large number of recorded Bragg peaks in combination with relatively low asymptotic intensity errors.

As already mentioned above, we additionally calculated the final lattice temperature T_{eq} by means of the absorbed pump fluence and graphite heat capacity according to [16]. The incident fluence was first determined by measuring the pump laser profile at an equivalent sample position outside of the vacuum chamber with a CCD beam profiler. Figure 13(d) illustrates the obtained fluence distribution, which is adequately uniform over the sample area with a maximum fluence deviation of less than 20%. Averaging over the entire sample area resulted in a mean incident pump fluence of $F = (6.2 \pm 0.4)$ mJ cm⁻². Fresnel's equations were further used to calculate an absorption of $A = (0.135 \pm 0.010)$ for the 3 nm multilayer graphene sample at 795 nm by taking into account its specific optical conductance [89] and the angle of incident onto the sample. Thus, an equilibrium lattice temperature of $T_{\text{eq}} = (1135 \pm 103)$ K could be finally determined from the incident pump fluence F by solving

$$F = \frac{d}{A} \int_{T_0}^{T_{\text{eq}}} C_p(T) dT, \quad (11)$$

with the temperature-dependent specific heat capacity per volume $C_p(T)$ of graphite taken from [90], the sample absorption A and corresponding thickness d .

Both results for the equilibrium lattice temperature, $T_{\text{eq}} = (1234 \pm 19)$ K from the Debye–Waller analysis of Bragg peak intensities and $T_{\text{eq}} = (1135 \pm 103)$ K from the absorbed pump laser fluence, agree within their error limits. In this connection, the quality of the time-resolved diffraction data is reflected in the considerable lower error of the resultant lattice temperature.

The presented time-resolved diffraction data on multilayer graphene could thus demonstrate that the studied excellent spatio-temporal resolution of our compact ultrafast electron diffractometer is unrestrictedly applicable for challenging future UED experiments.

4. Summary and conclusions

In this paper, we extensively investigated the interplay between spatial and temporal aspects of resolution limits in UED experiments on the basis of a newly designed, highly compact ultrafast electron diffractometer. The focus was directed to the robust generation of uncompressed multi-electron pulses with excellent spatio-temporal properties in the lower space charge regime as well as a successful application of these pulses to time-resolved experiments. In order to accomplish this, we have shown that the propagation distance of electron bunches from the source to the sample can be reduced threefoldly in comparison to so far most compact source designs by installing the magnetic lens behind the sample. Additionally, a static acceleration field strength above 10 MV m⁻¹ could be achieved with a pressed in, glue-free implementation of the photocathode substrate. These improvements diminish the longitudinal and lateral electron pulse broadening and allowed a reduction of the electron source size to extend the transverse coherence while maintaining an ultrashort pulse duration. Accordingly, we investigated the dependence of the electron source size and charge density on the transverse coherence length, electron pulse duration, diffraction signal intensity and instrumental brightness for reaching an optimized instrumental performance.

Three different electron source sizes were studied with a variation of the source area over more than two orders of magnitude. The transverse coherence length of the electron pulses was determined by three experimental approaches and a self-developed particle tracking program. Moreover, we directly extracted the transverse coherence length from the fitted widths of measured diffraction peaks. The smallest studied source sizes achieved the best coherence values up to 20 nm. By taking magnetic lens aberrations and a detector signal spreading into account, we revealed an up to sevenfold enlargement of Bragg peaks due to instrumental imperfections. However, a deconvolution via instrumental PSFs finally confirms the expected dependence of the Bragg peak intensity on the coherence. Our highly compact UED setup can therefore provide multi-electron pulses at the sample with a maximum transverse coherence length of about 20 nm while maintaining a bunch $1/e^2$ – radius of less than 85 μm .

Due to the fact that the coherence-improving source reduction inevitably increases space charge effects, we investigated the temporal pulse broadening as a function of the number of electrons per pulse for the three studied source sizes. Close to the single-electron regime, experimental as well as simulated outcomes have shown a minimal FWHM pulse duration of 120 fs for all source sizes resulting in overall temporal resolution of 60 fs (RMS). For 3000 electrons per bunch an outstanding RMS temporal resolution of 78 fs is reached using the largest investigated source radius at the cost of a low transverse coherence. Increasing the coherence to the highest value moderately reduces the RMS temporal resolution to 147 fs for ~ 1000 electrons per bunch.

On the basis of the spatio-temporal resolution studies, we further analysed influences on the diffraction signal intensity and electron pulse brightness. The expected quadratic dependence of the Bragg spot peak intensity with the transverse coherence length was only confirmed in absence of instrumental imperfections. Therefore, we extended the standard brightness definition to find optimal electron pulse settings for highest signal yields in space and time at a certain temporal resolution.

Finally, the full performance of our UED setup was demonstrated in a time-resolved experiment with optimized electron pulse parameters. We observed the in-plane lattice heating in multilayer graphene after ultrashort laser excitation and analysed the results by means of the Debye–Waller theory according to [16]. The high quality of the diffraction pattern thereby allowed the evaluation of 101 Bragg peaks at each pump–probe delay up to a reciprocal lattice vector of 18.4 \AA^{-1} . The statistical analysis of a selected Bragg peak intensity decay additionally demonstrated the high signal-to-noise ratio in the transient data. Thus, we conclude that the excellent spatio-temporal capability of the presented electron diffractometer is certainly applicable for many prospective UED experiments and we expect a high impact of this design on the field of ultrafast structural dynamics.

As an outlook this setup can be combined with ultrafast laser control techniques (see for example [91] and references therein) to study light–matter interaction with shaped laser pulses in order to guide material response towards user-designed directions.

Acknowledgments

We thank Jannik C Meyer for his introduction to graphite/graphene sample preparation techniques and Matthias Wollenhaupt for fruitful discussions during the initial phase of this project. Vanessa Sporleder and Xaver Holzapfel are gratefully acknowledged for their valued contributions to the temporal electron pulse characterization and SD-FROG measurements.

Appendix A. Transverse coherence definition

The transverse coherence length of an electron beam is a measure of the maximum resolvable distance in a sample over which the wave function describing the electrons is considered to be in phase. For an electron pulse with Gaussian phase space distribution, the transverse coherence length ξ_x along the lateral space coordinate x is often related to the standard deviations of the uncorrelated half-angle divergence $\sigma_{\theta,x}$ or local uncorrelated transverse momentum spread $\sigma_{p,x}$ by

$$\xi_x \equiv \frac{\lambda}{2\pi\sigma_{\theta,x}} = \frac{\hbar}{\sigma_{p,x}}, \quad (\text{A.1})$$

where \hbar is the reduced Planck constant and $\sigma_{\theta,x} = \sigma_{p,x}/p_z$ in the paraxial approximation with the mean longitudinal momentum p_z of the electrons. The transverse coherence length ξ_y along the lateral space coordinate y is given analogously. This definition is widely accepted in the field of UED [3, 5, 25, 40, 41, 54, 65].

From equation (A.1) directly follows an expression of the transverse coherence length ξ_x in terms of the local uncorrelated transverse wave vector spread $\sigma_{k,x}$ by

$$\xi_x = \frac{\hbar}{\sigma_{p,x}} = \frac{1}{\sigma_{k,x}}, \quad (\text{A.2})$$

where $\sigma_{p,x} = \hbar\sigma_{k,x}$. Here, the absolute value of the electron wave vector is defined by $|\mathbf{k}| = 2\pi/\lambda$, with the de Broglie wavelength λ . In case of an idealized diffraction experiment, without instrumental limitations and sample imperfections, the standard deviation of the Gaussian Bragg peaks in reciprocal space would be equal to the uncorrelated transverse wave vector spread $\sigma_{k,x}$ in equation (A.2) [25, 74, 92].

In state of the art UED experiments the transverse coherence length at the sample is typically orders of magnitude smaller than the lateral electron pulse diameter [4, 5] and the global correlated half-angle divergence is about a few mrad (≤ 4 mrad in our setup). Under this conditions the transverse coherence length ξ_x is only marginally reduced by the correlated angle divergence and can be well approximated analogously to equation (A.1) by means of the transverse emittance $\varepsilon_{n,x}$ as follows: In regions of a setup where the electron pulses are focused or collimated, the correlated angle divergence vanishes and the normalized RMS emittance $\varepsilon_{n,x}$ of equation (2) can be reduced to

$$\varepsilon_{n,x} = \frac{\sigma_x \sigma_{p,x}}{m_0 c} = \frac{w_x \sigma_{p,x}}{2m_0 c}, \quad (\text{A.3})$$

with the standard deviation σ_x of the spatial electron pulse profile along the lateral coordinate x , the equivalent pulse $1/e^2$ -radius $w_x = 2\sigma_x$, the uncorrelated transverse momentum spread $\sigma_{p,x}$, the electron rest mass m_0 and the speed of light c [5, 41, 65]. The emittance $\varepsilon_{n,y}$ for the lateral coordinate y is given analogously. Hence, the combination of equations (A.1) and (A.3) results in the approximation of the transverse coherence length ξ_x through the normalized emittance $\varepsilon_{n,x}$ [5, 41, 65],

$$\xi_x \approx \frac{\hbar}{m_0 c} \frac{w_x}{2\varepsilon_{n,x}}. \quad (\text{A.4})$$

This approximation has been used in our particle tracking algorithm instead of equation (A.2) due to a higher numerical robustness and insignificant deviations in the studied parameter regime.

Appendix B. Particle tracking simulation

A particle tracking program was self-developed to get direct access to all tuneable electron pulse parameters and their effects on the spatio-temporal resolution of our UED setup. 3D charged particle trajectories were calculated under the combined influence of instrumental electromagnetic fields and space charge forces by grouping electrons inside a pulse to so-called macroparticles [93]. A single pulse has been typically simulated by means of 1000 macroparticles regardless of the number of electrons per pulse to allow significant statistical analyses and to give a feasible estimation of the space charge effects for pulses with less than 5000 electrons. Accordingly, each macroparticle has to carry a defined fraction of charge (at a constant mass-to-charge ratio) so that the entire electron pulse charge is fully represented. The macroparticles relativistic equations of motion have been solved by the velocity-Störmer-Verlet method, a standard symplectic integrator in molecular dynamics simulations [94]. The trajectories of the macroparticles after the emission process (see section B.1) have been typically simulated in pre-optimized time steps of 100 fs. The electric field of the acceleration region including the inhomogeneous field distribution around the anode pinhole (see figure 3 and section 3.1) was implemented by means of an analytically approximation given in [95]. The involved magnetic field distribution of the solenoid (see figure 7 and section 3.1) was determined from engineering data by the freely available FEMM finite element program [75]. Space charge forces between the 1000 macroparticles have been calculated relativistically by a 3D point-to-point model [93]. Only Lorentz contraction was not considered within the space charge model [93], which results for our experimental conditions in a more than fourfold simulation speed-up at less than 0.4% deviations from a full implementation of relativistic effects. The accuracy of the particle tracking program was additionally validated with Gaussian electron test pulses against the analytical Gaussian model developed by Michalik *et al* [92, 96].

B.1. Initial phase space distribution

Apart from space charge effects, the initial electron pulse phase space distribution directly after photoemission constitutes all important spatio-temporal pulse properties at the sample. Thus, an accurate imitation of the initial phase space distribution is essential to achieve a successful reproduction of experimental pulse parameters by means of the particle tracking simulation. The starting point is the random assignment of initial 3D positions and momenta to the macroparticles from the predefined phase space distribution. Thereby, the transverse spatial electron distribution has been assumed to have a Gaussian shape whose $1/e^2$ -radius is given by the UV laser spot size on the photocathode (see section 3). The longitudinal spatial distribution and therefore the

temporal shape of the electron pulse has been represented by a Gaussian profile as well. The emission of each macroparticle within the UV laser pulse duration (30 fs (FWHM)) has been simulated with a temporal resolution of 120 as. In this process, electromagnetic fields and space charge effects are already taken into account. The initial velocity distribution has been calculated via the three step model of photoemission in accordance with [61, 64]. The shape of the velocity distribution is thereby defined due to the following intrinsic instrumental parameters: UV pulse central photon energy $\hbar\omega = (4.64 \pm 0.03)$ eV, gold cathode workfunction $\phi_0 = (4.26 \pm 0.2)$ eV from [51, 64] and electric acceleration field strength $E_{\text{acc}} = U/d = (11.4 \pm 0.7)$ MV m⁻¹ with $U = 40$ kV (10^{-4} relative stability) and $d = (3.5 \pm 0.2)$ mm. Furthermore, these instrumental parameters allow an analytical approximation of the intrinsic normalized emittance $\varepsilon_{n,i}$ from the following expression [61–63]

$$\varepsilon_{n,i} = \frac{w_i}{2} \sqrt{\frac{\hbar\omega - \phi_{\text{eff}}}{3m_0c^2}}, \quad (\text{B.1})$$

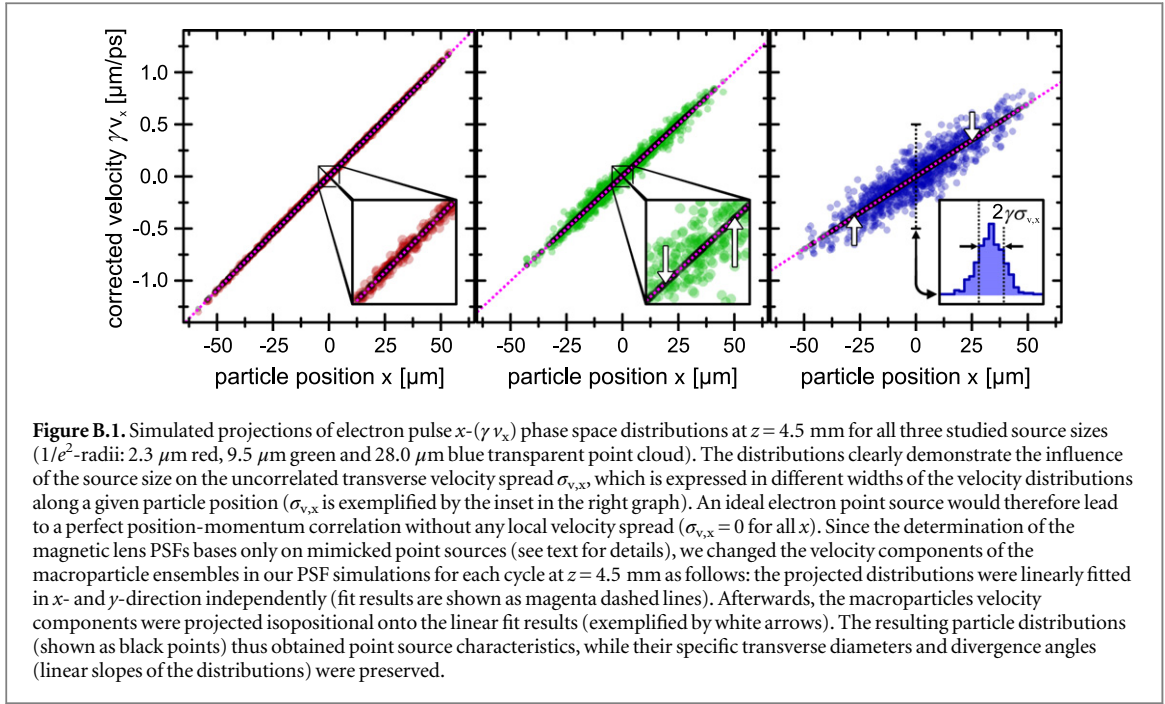
with the electron source $1/e^2$ -radius w_i , the laser photon energy $\hbar\omega$, the effective work function ϕ_{eff} , the electron rest mass m_0 and the speed of light c . Here, the effective work function $\phi_{\text{eff}} = \phi_0 - \sqrt{e^3 E_{\text{acc}} / 4\pi\epsilon_0}$ is the cathode work function ϕ_0 lowered by the Schottky effect [61, 62], where e is the elementary charge, E_{acc} is the electric acceleration field strength and ϵ_0 is the vacuum permittivity. Thus, the combination of equation (B.1) with equation (A.4) results in an initial transverse coherence length of $\xi_i = (0.67 \pm 0.16)$ nm for our setup, which provides the basis for further transverse coherence analyses in section 3.1.

B.2. Simulating the PSF of the magnetic lens

In section 3.1, magnetic lens PSFs are used to quantify the source-limited transverse coherence lengths in dependence of the electron pulse source size. The determination procedure of the magnetic lens PSFs for all three studied source sizes is described in the following.

For each of the finite source sizes, the experimental conditions were first reconstructed by tracing the overall propagation of macroparticle bunches (always representing 1500 electrons per pulse) from their point of generation at the cathode to the detector plane, including the diffraction process in \hat{z} direction of the graphene sample (see figure 7). In these simulations, the minimal spot size of the resulting \hat{z} Bragg peak on the detector could be well retrieved by optimizing a scale factor for the global magnetic field strength. It should be noted that for all source sizes the optimal scale factors differed less than 10% from the parameter-free finite element results of the FEMM program (see also figure 7). The actual determination of the PSFs was based on the reconstruction of the experimental fields.

Influenced by lens aberrations and space charge effects, a magnetic lens PSF simply represents the focussed intensity distribution of an electron point source on the detector. However, particularly within the space charge regime, an ideal point source is not realizable. Therefore, we determined the magnetic lens PSFs by mimicking point sources in the following way: Electron pulses from a finite source area were propagated until 1 mm behind the anode at $z = 4.5$ mm, where the electric acceleration field and magnetic lens fields are both negligible (see figures 3 and 7). At this point the projection of the lateral phase space distribution (shown in figure B.1 for the lateral coordinate x) clearly demonstrates the influence of the source size on the uncorrelated transverse velocity spread $\sigma_{v,x}$ (standard deviation of the velocity distribution along a given position x). This velocity spread $\sigma_{v,x}$ is directly related to the uncorrelated transverse momentum spread $\sigma_{p,x} = m_0 \gamma \sigma_{v,x}$ via the electron rest mass m_0 and the Lorentz factor γ . The momentum spread $\sigma_{p,x}$ further defines the transverse coherence length of the electron pulse (see appendix A for details). To finally achieve a macroparticle ensemble with point source properties, we altered the phase space distributions at $z = 4.5$ mm as follows: The projected distributions were linearly fitted independently in x - and y -direction and then the transverse velocity components of each macroparticle were set to the values of the linear fit functions at its position (see figure B.1 for details). This modification creates a laterally fully coherent electron pulse with a perfect linear position-momentum correlation like bunches from an electron point source. In addition, the method preserves the specific transverse diameter and divergence angle of the electron pulses from each of the three studied source sizes. The further propagation of the fully coherent electron pulses to the detector plane at $z = 188$ mm was simulated similarly to the finite source case above under the influence of diffraction and the predetermined optimal magnetic field strength. The final intensity distributions of the magnetic lens PSFs were achieved by integrating over 1000 single simulations cycles, while each macroparticle ensemble represented 1500 electrons per pulse.



B.3. Instrumental brightness definition

According to [66, 97], the transverse normalized peak brightness B_n is defined by

$$B_n \equiv \frac{I_0}{4\pi^2 \varepsilon_{n,x} \varepsilon_{n,y}}, \quad (\text{B.2})$$

with the peak current I_0 and the transverse normalized emittance ε_n in x - and y -direction given by equation (2). Due to the cylindrical symmetry of our apparatus we have $\varepsilon_{n,x} = \varepsilon_{n,y} = \varepsilon_n$. The factor $4\pi^2$ originates from the assumption of a transverse 4D Gaussian shaped phase space distribution. Assuming a Gaussian profile for the longitudinal pulse distribution as well, the peak current I_0 is given by

$$I_0 \equiv \frac{Ne}{\sqrt{2\pi} \sigma_\tau}, \quad (\text{B.3})$$

where N is the number of electrons per pulse, σ_τ is the electron pulse duration (standard deviation) and e is the elementary charge. From equation (A.4) follows an approximation of the normalized emittance ε_n by the use of the source-limited transverse coherence length ξ_s and $1/e^2$ -radius of electron pulse w_s at the sample. Taking into account that the source-limited coherence ξ_s is normally reduced by instrumental imperfections to the instrumental coherence ξ_1 (see sections 3.1 and 3.3 for details), the instrumental transverse normalized peak brightness B_1 is finally given from the combination of the above equations (B.2), (B.3) and (A.4)

$$B_1 \approx \left(\frac{m_0 c}{\pi \hbar} \right)^2 \sqrt{\frac{8 \ln 2}{2\pi}} \frac{Ne \xi_1^2}{\tau_e w_s^2}, \quad (\text{B.5})$$

where the standard deviation σ_τ of the electron pulse duration is additionally replaced by the FWHM duration $\tau_e = \sqrt{8 \ln 2} \sigma_\tau$.

References

- [1] Chergui M and Zewail A H 2009 *ChemPhysChem* **10** 28–43
- [2] Miller R J D 2014 *Science* **343** 1108–16
- [3] Sciaini G and Miller R J D 2011 *Rep. Prog. Phys.* **74** 096101
- [4] Carbone F, Musumeci P, Luiten O J and Hebert C 2012 *Chem. Phys.* **392** 1–9
- [5] Baum P 2013 *Chem. Phys.* **423** 55–61
- [6] Vartanyants I A et al 2011 *Phys. Rev. Lett.* **107** 144801
- [7] Williamson J C, Cao J, Thee H, Frey H and Zewail A H 1997 *Nature* **386** 159–62
- [8] Thee H, Lobastov V A, Gomez U M, Goodson B M, Srinivasan R, Ruan C-Y and Zewail A H 2001 *Science* **291** 458–62
- [9] Park S T, Gahlmann A, He Y, Feenstra J S and Zewail A H 2008 *Angew. Chem., Int. Ed. Engl.* **120** 9638–41
- [10] Hensley C J, Yang J and Centurion M 2012 *Phys. Rev. Lett.* **109** 133202
- [11] Siwick B J, Dwyer J R, Jordan R E and Miller R J D 2003 *Science* **302** 1382–5
- [12] Ernstorfer R, Harb M, Hebeisen C T, Sciaini G, Dartigalongue T and Miller R J D 2009 *Science* **323** 1033–7

- [13] Sciaini G, Harb M, Kruglik S G, Payer T, Hebeisen C T, Meyer zu Heringdorf F-J, Yamaguchi M, Horn-von Hoegen M, Ernstorfer R and Miller R J D 2009 *Nature* **458** 56–9
- [14] Carbone F, Baum P, Rudolf P and Zewail A H 2008 *Phys. Rev. Lett.* **100** 035501
- [15] Raman R K, Murooka Y, Ruan C-Y, Yang T, Berber S and Tomanek D 2008 *Phys. Rev. Lett.* **101** 077401
- [16] Schäfer S, Liang W and Zewail A H 2011 *New J. Phys.* **13** 063030
- [17] Gerbig C, Morgenstern S, Sarpe C, Wollenhaupt M and Baumert T 2012 *Research in Optical Sciences* (Washington, DC: OSA) p IT3D.3
- [18] Lahme S, Kealhofer C, Krausz F and Baum P 2014 *Struct. Dyn.* **1** 034303
- [19] Chatelain R P, Morrison V R, Klarenaar B L M and Siwick B J 2014 *Phys. Rev. Lett.* **113** 235502
- [20] Eichberger M, Schäfer H, Krumova M, Beyer M, Demsar J, Berger H, Moriena G, Sciaini G and Miller R J D 2010 *Nature* **468** 799–802
- [21] Erasmus N, Eichberger M, Haupt K, Boshoff I, Kassier G, Birmurske R, Berger H, Demsar J and Schwoerer H 2012 *Phys. Rev. Lett.* **109** 167402
- [22] Gao M et al 2013 *Nature* **496** 343–6
- [23] Gulde M, Schweda S, Storeck G, Maiti M, Yu H K, Wodtke A M, Schäfer S and Ropers C 2014 *Science* **345** 200–4
- [24] Siwick B J, Dwyer J R, Jordan R E and Miller R J D 2004 *Chem. Phys.* **299** 285–305
- [25] Gahlmann A, Park S T and Zewail A H 2008 *Phys. Chem. Chem. Phys.* **10** 2894–909
- [26] Harb M, Ernstorfer R, Hebeisen C T, Sciaini G, Peng W, Dartigalongue T, Eriksson M A, Lagally M G, Kruglik S G and Miller R J D 2008 *Phys. Rev. Lett.* **100** 155504
- [27] Ligges M, Rajkovic I, Zhou P, Posth O, Hassel C, Dumpich G and von der Linde D 2009 *Appl. Phys. Lett.* **94** 101910
- [28] Nie S, Wang X, Li J, Clinite R and Cao J 2009 *Microsc. Res. Tech.* **72** 131–43
- [29] Kassier G H, Haupt K, Erasmus N, Rohwer E G, von Bergmann H M, Schwoerer H, Coelho S M M and Auret F D 2010 *Rev. Sci. Instrum.* **81** 105103
- [30] Chatelain R P, Morrison V R, Godbout C and Siwick B J 2012 *Appl. Phys. Lett.* **101** 081901
- [31] Gao M, Jean-Ruel H, Cooney R R, Stampe J, de Jong M, Harb M, Sciaini G, Moriena G and Miller R J D 2012 *Opt. Express* **20** 12048–58
- [32] Mancini G F, Mansart B, Pagano S, van der Geer B, de Loos M and Carbone F 2012 *Nucl. Instrum. Methods Phys. Res. A* **691** 113–22
- [33] Hommelhoff P, Sortais Y, Aghajani-Talesh A and Kasevich M A 2006 *Phys. Rev. Lett.* **96** 077401
- [34] Ropers C, Solli D R, Schulz C P, Lienau C and Elsaesser T 2007 *Phys. Rev. Lett.* **98** 043907
- [35] Paarmann A et al 2012 *J. Appl. Phys.* **112** 113109
- [36] Quinonez E, Handali J and Barwick B 2013 *Rev. Sci. Instrum.* **84** 103710
- [37] Hoffrogge J, Stein J P, Krüger M, Förster M, Hammer J, Ehberger D, Baum P and Hommelhoff P 2014 *J. Appl. Phys.* **115** 094506
- [38] Claessens B J, van der Geer S B, Taban G, Vredenburg E J D and Luiten O J 2005 *Phys. Rev. Lett.* **95** 164801
- [39] McCulloch A J, Sheludko D V, Saliba S D, Bell S C, Junker M, Nugent K A and Scholten R E 2011 *Nat. Phys.* **7** 785–8
- [40] Saliba S D, Putkunz C T, Sheludko D V, McCulloch A J, Nugent K A and Scholten R E 2012 *Opt. Express* **20** 3967–74
- [41] Engelen W J, van der Heijden M A, Bakker D J, Vredenburg E J D and Luiten O J 2013 *Nat. Commun.* **4** 1693
- [42] van Mourik M W, Engelen W J, Vredenburg E J D and Luiten O J 2014 *Struct. Dyn.* **1** 034302
- [43] van Oudheusden T, Pasmans P L E M, van der Geer S B, de Loos M J, van der Wiel M J and Luiten O J 2010 *Phys. Rev. Lett.* **105** 264801
- [44] Hastings J B, Rudakov F M, Dowell D H, Schmerge J F, Cardoza J D, Castro J M, Gierman S M, Loos H and Weber P M 2006 *Appl. Phys. Lett.* **89** 184109
- [45] Li R, Tang C, Du Y, Huang W, Du Q, Shi J, Yan L and Wang X 2009 *Rev. Sci. Instrum.* **80** 083303
- [46] Musumeci P, Moody J T, Scoby C M, Gutierrez M S and Westfall M 2010 *Appl. Phys. Lett.* **97** 063502
- [47] Murooka Y, Naruse N, Sakakihara S, Ishimaru M, Yang J and Tanimura K 2011 *Appl. Phys. Lett.* **98** 251903
- [48] Hebeisen C T, Sciaini G, Harb M, Ernstorfer R, Dartigalongue T, Kruglik S G and Miller R J D 2008 *Opt. Express* **16** 3334–41
- [49] Tokita S, Hashida M, Inoue S, Nishoji T, Otani K and Sakabe S 2010 *Phys. Rev. Lett.* **105** 215004
- [50] Kassier G H, Erasmus N, Haupt K, Boshoff I, Siegmund R, Coelho S M M and Schwoerer H 2012 *Appl. Phys. B* **109** 249–57
- [51] Aidelsburger M, Kirchner F O, Krausz F and Baum P 2010 *Proc. Natl Acad. Sci. USA* **107** 19714–9
- [52] Michalik A M, Sherman E Y and Sipe J E 2008 *J. Appl. Phys.* **104** 054905
- [53] Kirchner F O, Lahme S, Krausz F and Baum P 2013 *New J. Phys.* **15** 063021
- [54] van Oudheusden T, de Jong E F, van der Geer S B, Op't Root W P E M, Luiten O J and Siwick B J 2007 *J. Appl. Phys.* **102** 093501
- [55] Graf U, Fieß M, Schultze M, Kienberger R, Krausz F and Goulielmakis E 2008 *Opt. Express* **16** 18956–63
- [56] Meyer J C, Girit C O, Crommie M F and Zettl A 2008 *Appl. Phys. Lett.* **92** 123110
- [57] Novoselov K S, Geim A K, Morozov S V, Jiang D, Zhang Y, Dubonos S V, Grigorieva I V and Firsov A A 2004 *Science* **306** 666–9
- [58] Blake P, Hill E W, Castro Neto A H, Novoselov K S, Jiang D, Yang R, Booth T J and Geim A K 2007 *Appl. Phys. Lett.* **91** 063124
- [59] Bazarov I V, Dunham B M and Sinclair C K 2009 *Phys. Rev. Lett.* **102** 104801
- [60] Filippetto D, Musumeci P, Zolotorev M and Stupakov G 2014 *Phys. Rev. ST Accel. Beams* **17** 024201
- [61] Dowell D H and Schmerge J F 2009 *Phys. Rev. ST Accel. Beams* **12** 074201
- [62] Hauri C P, Ganter R, Le Pimpec F, Trisorio A, Ruchert C and Braun H H 2010 *Phys. Rev. Lett.* **104** 234802
- [63] Rickman B L, Berger J A, Nicholls A W and Schroeder W A 2013 *Phys. Rev. Lett.* **111** 237401
- [64] Tao Z, Zhang H, Duxbury P M, Berz M and Ruan C-Y 2012 *J. Appl. Phys.* **111** 044316
- [65] Kassier G H, Haupt K, Erasmus N, Rohwer E G and Schwoerer H 2009 *J. Appl. Phys.* **105** 113111
- [66] van der Geer S B, de Loos M J, van Oudheusden T, Op't Root W P E M, van der Wiel M J and Luiten O J 2006 *Phys. Rev. ST Accel. Beams* **9** 044203
- [67] Li R K, Roberts K G, Scoby C M, To H and Musumeci P 2012 *Phys. Rev. ST Accel. Beams* **15** 090702
- [68] Strehl P 2006 *Beam Instrumentation and Diagnostics (Particle Acceleration and Detection)* ed A Chao et al (Berlin: Springer)
- [69] Tate M W, Chamberlain D and Gruner S M 2005 *Rev. Sci. Instrum.* **76** 081301
- [70] Castelli C M, Allinson N M, Moon K J and Watson D L 1994 *Nucl. Instrum. Methods Phys. Res. A* **348** 649–53
- [71] Spence J C H 2009 *High-Resolution Electron Microscopy* ed R J Brook et al (Oxford: Oxford University Press)
- [72] Fultz B and Howe J 2013 *Transmission Electron Microscopy and Diffractometry of Materials (Graduate Texts in Physics)* ed W T Rhodes et al (Heidelberg: Springer)
- [73] Ghadimi R, Daberkow I, Kofler C, Sparlinek P and Tietz H 2011 *Microsc. Microanal.* **17** 1208–9
- [74] Li R K, Musumeci P, Bender H A, Wilcox N S and Wu M 2011 *J. Appl. Phys.* **110** 074512
- [75] Meeker D C 2013 Finite Element Method Magnetics 4.2 64-bit (25 August 2013 Build)(www.femm.info)
- [76] Wiza J L 1979 *Nucl. Instrum. Methods* **162** 587–601
- [77] Kirchner F O, Gliserin A, Krausz F and Baum P 2014 *Nat. Photonics* **8** 52–7
- [78] Plemmons D A, Park S T, Zewail A H and Flannigan D J 2014 *Ultramicroscopy* **146** 97–102

- [79] Morrison V R, Chatelain R P, Godbout C and Siwick B J 2013 *Opt. Express* **21** 21–9
- [80] Scheuch M, Kampfrath T, Wolf M, von Volkman K, Frischkorn C and Perfetti L 2011 *Appl. Phys. Lett.* **99** 211908
- [81] Breusing M, Ropers C and Elsaesser T 2009 *Phys. Rev. Lett.* **102** 086809
- [82] Yan H, Song D, Mak K F, Chatzakos I, Maultzsch J and Heinz T F 2009 *Phys. Rev. B* **80** 121403
- [83] Carbone F, Aubock G, Cannizzo A, van Mourik F, Nair R R, Geim A K, Novoselov K S and Chergui M 2011 *Chem. Phys. Lett.* **504** 37–40
- [84] Ishida Y, Togashi T, Yamamoto K, Tanaka M, Taniuchi T, Kiss T, Nakajima M, Suemoto T and Shin S 2011 *Sci. Rep.* **1** 64
- [85] Tao Z, Han T-R T and Ruan C-Y 2013 *Phys. Rev. B* **87** 235124
- [86] Warren B E 1990 *X-Ray Diffraction* (New York: Dover) pp 189–92
- [87] Chen R and Trucano P 1978 *Acta Crystallogr. A* **34** 979–82
- [88] Tohei T, Kuwabara A, Oba F and Tanaka I 2006 *Phys. Rev. B* **73** 064304
- [89] Skulason H S, Gaskell P E and Szkopek T 2010 *Nanotechnology* **21** 295709
- [90] Butland A T D and Maddison R J 1973 *J. Nucl. Mater.* **49** 45–56
- [91] Wollenhaupt M and Baumert T 2011 *Faraday Discuss.* **153** 9–26
- [92] Michalik A M and Sipe J E 2009 *J. Appl. Phys.* **105** 084913
- [93] van der Geer S B and de Loos M J 2001 The general particle tracer code: design, implementation and application *PhD Thesis* Technische Universiteit Eindhoven
- [94] Griebel M, Knappek S and Zumbusch G 2007 *Numerical Simulation in Molecular Dynamics: Numerics, Algorithms, Parallelization, Applications (Texts in Computational Science and Engineering vol 5)* ed T J Barth et al (Berlin: Springer) pp 43–5
- [95] Hawkes P W and Kasper E 1989 Principles of electron optics *Applied Geometrical Optics vol 2* (London: Academic) p 632
- [96] Michalik A M and Sipe J E 2006 *J. Appl. Phys.* **99** 054908
- [97] Brau C A 2003 What brightness means *The Physics and Applications of High Brightness Electron Beams Proc. ICFA Workshop 2002* ed J Rosenzweig et al (Singapore: World Scientific) pp 20–7